11-16-2012

Micro-extrusion process parameter modeling

Anuj Datar

Micro-extrusion Process Parameter Modeling

Anuj Datar

Thesis submitted to the Faculty of the

Rochester Institute of Technology

In partial fulfillment of the requirements for the degree of

Master of Science

in

Industrial Engineering

Thesis Committee

Dr. Denis Cormier

Dr. Marcos Esterman

Department of Industrial and Systems Engineering

11/16/2012

DEPARTMENT OF INDUSTRIAL AND SYSTEMS ENGINEERING

KATE GLEASON COLLEGE OF ENGINEERING

ROCHESTER INSTITUTE OF TECHNOLOGY

ROCHESTER, NEW YORK

CERTIFICATE OF APPROVAL

November 16, 2012

M.S. DEGREE THESIS

The M.S. Degree Thesis of Anuj Datar

has been examined and approved by the

thesis committee as satisfactory for the

thesis requirement for the

Master of Science degree

Approved by:

Dr. Denis Cormier, Thesis Advisor

Dr. Marcos Esterman, Committee Member

Abstract

Direct write processes are a family of technologies with the ability to deposit functional structures directly onto planar and non-planar surfaces. Direct writing includes a variety of processes that use different mechanisms to transfer materials on to substrates and can be generally distinguished from conventional rapid prototyping processes by a feature resolution in the sub-micron to micron range. The dispensing system studied in this thesis is a pneumatically actuated micro-extruder which is capable of processing a wide variety of materials. This material dispensing tool is capable of depositing small amounts of material to build three dimensional structures in an accurate and repeatable manner. The material dispensing system in this study has a variety of manufacturing applications ranging from printed electronics to biomedical applications.

The material dispensing system employs a needle valve mechanism that allows ink or slurry to be deposited onto a substrate using air pressure. The dispensing tool used for this research is an nScrypt SmartPump. This research is focused on analyzing the extrusion process and developing and validating a parametric model for the input parameters using a design of experiments (DOE) approach. The aim is to improve the repeatability and accuracy of the process.

A two phase approach was used to identify significant input parameters impacting the dimensional properties of a printed track. The first set of experiments employed a 2-level fractional factorial screening design where all user controllable parameters were tested against the response variables – height and width of a printed track. Significant parameters from this analysis were then used to build a regression equation for both height and width. It was observed that while the regression equation for height was accurate in predicting the output at intermediate levels, the regression equation for width was unable to do so and displayed signs of curvature. A higher order three-level regression model was then fit to the significant parameters for width and was found to be satisfactory in predicting process output. The errors observed between predicted outputs from the regression equations and actual output dimensions from the validation experiments were less than 2% and 3% for height and width respectively.

Acknowledgements

First and foremost I would like to thank Dr. Denis Cormier, for his guidance and support throughout my master's degree. Without his input and inspiration, this thesis would not have been possible. I am grateful to have had the opportunity to learn from him and work with him on the HeteroFoaM research project. I would also like to thank Dr. Marcos Esterman for his patience and the invaluable guidance he provided during the course of my thesis. I would like to express my gratitude towards the Industrial and Systems Engineering Department for their help and support over the last three years.

I would like to thank my lab mates Sundaresan Balasubramanian, Prasanna Khatri-Chhetri, Niranjan Damle Hrushikesh Godbole, and Matt Purcell, who made working in the lab such a wonderful experience. I would also like to thank my friends Tejas, Kaushik, Sujay, Bhavesh, Vignesh, Ashish, Kamlesh and many others whose names are not in the list, for making my stay at Rochester enjoyable and memorable.

Finally, I would like to thank my parents Surekha and Vishwas Datar and my brother Akshay for their unwavering faith and support. Without them this would not have been possible.

This work was supported by Heterogeneous Functional Materials Center (HeteroFoaM), an Energy Frontier Research Center (EFRC) funded by the U. S. Department of Energy and Office of Basic Energy Sciences under award number DE-SC0001061.

Contents

List of Figures

List of Tables

Chapter 1

Introduction

1.1 Additive Manufacturing

Additive manufacturing (AM), also known as solid freeform fabrication (SFF), refers to a group of technologies wherein a part is manufactured directly from graphical computer data [1]. Additive manufacturing techniques work by virtually slicing 3D CAD models into a series of cross-sections, or layers with finite thickness. Material is then deposited one layer at a time to build up a part. This gives one the latitude of building complex 3D parts that are otherwise either difficult or impossible to produce using conventional manufacturing methods like CNC machining. Additive manufacturing is often referred to as Rapid Prototyping. These techniques generally eliminate the lead time necessary to design and manufacture specialized tools or dies required during the product design and development process.

Stereolithography was the first of such techniques, developed in the mid 1980's [2, 3]. Since then, several technologies have emerged that enable the use of a variety of materials. Additive manufacturing techniques can be classified in many ways based on materials, processes, tools, etc. Additive manufacturing techniques can be classified as solid, liquid, and powder based processes. Solid based processes include sheet based processes; liquid based processes include photo-polymerization processes, extrusion based processes, and printing processes; powder based processes include powder bed fusion processes, and beam deposition processes [2, 4].

Stereolithography, a process developed by 3D Systems, works on the principle of photo-polymerization where a laser scans the surface of a photo-sensitive resin curing one layer at a time. Fused deposition modeling, developed by Stratasys Inc., works by melting a thermoplastic material and extruding this molten material through a nozzle. Inkjet printing has been used to deposit a variety of materials, for example powders (metals, ceramics) suspended in liquids, metals with low melting points, wax, photo-sensitive polymers, proteins and others [5]. Another process that uses inkjet printing, known as 3D printing, works by printing droplets of binders onto powder beds of metals, ceramics, etc. 3D printing was developed at MIT [4]. The underlying principle is the same as any ordinary inkjet printer. A piezo electric

or a thermal print head is used to print drops of a liquid material that has a viscosity similar to that of water.

Beam deposition systems and powder bed fusion processes are similar in the fact that they both use energy beams like electron-beams or lasers. Beam deposition systems melt material while it is being deposited, whereas powder bed fusion processes melt material in a pre-laid bed of powder. Laser sintering has the ability to work with a large number of materials including metals, ceramics, polymers, etc. [2, 4, 6, 7], while electron beams can only be used for conducting materials[2]. Extrusion based processes involve extruding a gel or paste like material through an orifice or nozzle. In processes like fused deposition modeling a solid is melted and the resulting liquid is extruded through a nozzle [2, 4]. Extrusion based processes have been used to deposit bio materials for host frameworks called scaffolds for tissue formation [2, 8]. Sheet lamination processes use different mechanisms to bond sheets of material and cut the individual sheets or the stack [2].

1.1.1 Applications of Additive Manufacturing

Additive manufacturing (AM) has a wide variety of applications. Initially additive manufacturing was used to create visualization models, i.e. prototypes for products as they were being developed, as physical models are more useful than drawings or CAD renderings in the design process. Hence these processes were initially termed rapid prototyping. As technologies developed and improved, the number of applications for AM increased. AM, when used in conjunction with other technologies to form process chains, can be used to significantly shorten product development times and costs. For example, parts fabricated using conventional CNC machining or even 3D printing used in conjunction with maskless deposition of electronic circuits can be used to fabricate functional prototypes in a short duration. Certain AM technologies have been developed to the point where their output is suitable for end use. Some technologies have also been adapted for mass production. For example, Invisalign braces by Align Technology Inc. are mass produced dental braces using 3D printing. The ability to use lasers and energy beams to process metals has greatly increased the possibilities and applications for AM. Some applications of AM include biological or human implants such as hip, dental replacements, custom bone implants, forensics, electronics, rapid tooling etc.

1.1.2 The Generic Additive Manufacturing Process

In order to manufacture an object using additive manufacturing, the first step is to create a CAD model (solid or surface representation) of the object. This can be done using a professional CAD package or by reverse engineering techniques such as laser scanning, CT scanning, etc. The next step is to export or convert this model to the .STL file format. STL files represent the surface of a solid or surface model using triangles. Coordinates of these triangles are stored in a text or binary file [3]. This STL format is used by most additive manufacturing processes. Next this .STL file is sliced into a series of layers of finite thickness based on the height resolution of the process. This file now is ready to be transferred to the machine controller for tool manipulation. Once the machine is set up with the right materials, the parameters are set and the sliced .STL file is loaded, the build process is initiated. Most machines are automated and only require superficial monitoring during the build process. Once building is complete, the part has to be removed from the machine. Some processes produce functional parts that can be used right out of the machine, while others require a certain degree of post processing. Post processing may include cleaning, removal of support material, a finishing operation, a surface treatment operation, heat treatment, etc. Now the part is ready for use.

Certain geometries, such as overhangs or delicate geometries, have a tendency to curl or fall apart during the build process. These geometries cannot be produced without the use of proper support structures. Fused deposition modeling by Stratasys utilizes a water soluble support material. In processes where powder beds or resin reservoirs are used, the powder bed or reservoir themselves perform the function of supporting structures. For such parts, a post processing step is required where support material is removed and the part is cleaned. This is especially important in cases where these parts may be used for biomedical application such as implants, or with Stereolithography parts where the photo-polymer can be a health hazard.

1.2 Direct Write

Direct write (DW) is a subgroup of additive manufacturing technologies that have the ability to build up structures on any functional surface, planar or non-planar, without any masking or tooling. These techniques are generally associated with feature resolution in the micron range [2, 9, 10]. Employing several mechanisms these techniques can process a variety of materials, from metals, ceramics, polymers to electrically and optically functional materials [9]. DW processes can be broadly classified as droplet based processes, laser and energy beam based processes, tip based processes and flow based processes. The different types of DW processes are discussed below.

1.2.1 Droplet Based Processes

Inkjet printing processes

Inkjet printing usually involves deposition of droplets of liquid precursor inks which solidify post printing due to evaporation, cooling, chemical reactions, or other post processing. These processes are similar to inkjet printing from additive manufacturing, but are mainly used to deposit thin layers of material, usually electrically conducting circuits, on relatively flat surfaces rather than to build up height [2]. There are two methods commonly used to generate droplets. These are continuous inkjet, and drop on demand inkjet heads [9]. The continuous mode (CIJ), as shown in Figure 1(a) has a steady stream of electrically charged ink droplets that are deflected onto a substrate electrostatically. The amount of charge induced and the amount of deflection produced in each droplet is controlled by electrostatic fields generated between electrodes. Uncharged particles fall back into a gutter and are recycled through the system. The drop on demand (DOD) method, as shown in Figure 1(b) ejects drops of ink only when the system is required to print. Liquid is ejected using either a thermal or a piezoelectric actuator using trigger signals.

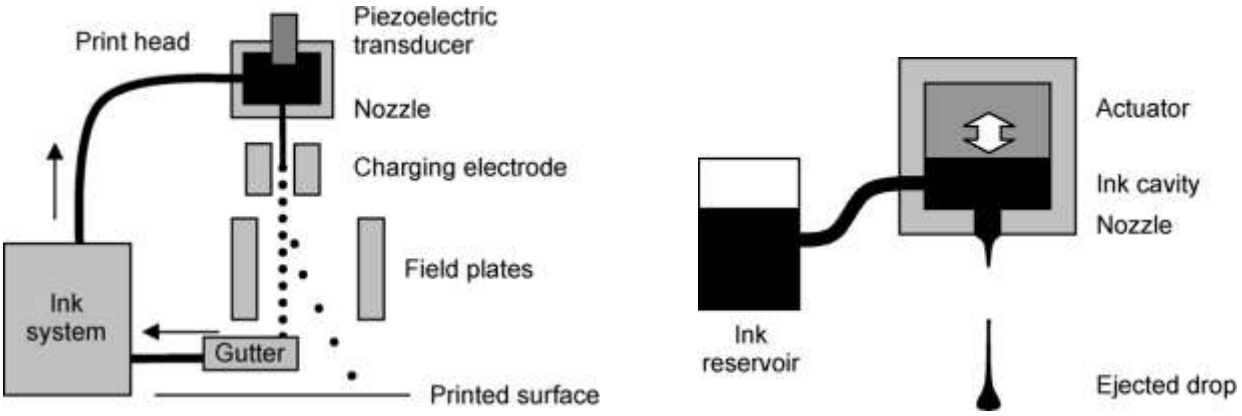

(a) (b)

Figure 1: (a) Continuous ink jetting (CIJ) system; (b) Drop-on-demand (DOD) inkjet system [9]

Aerosol-Jet deposition

Aerosol-Jet direct write deposits material in the form of a jet or beam of aerosol mist. It works by atomizing an ink, precursor or a colloidal suspension, and then delivering this aerosol mist in a stream of carrier gas to the deposition head where it exits a nozzle as a focused beam onto a substrate which may or

may not be conformal. Originally developed by Optomec with the name Maskless Mesoscale Material Deposition (M3D), this system utilizes pneumatic or ultrasonic mechanisms to atomize inks based on ink properties. The system uses nitrogen as the carrier gas, as N_2 is chemically stable and does not react easily with most materials used in the process. Other carrier gases have been used in research as well. The carrier gas is used to transport aerosol mist from the atomizer to the deposition head. A separate stream of this carrier gas is also used to create annular flow at the nozzle to focus and collimate the Aerosol-Jet and to provide precise control over printed tracks while maintaining zero contact of material with the nozzle, thus avoiding clogging. Figure 2 shows a schematic diagram of the Aerosol-Jet deposition process.

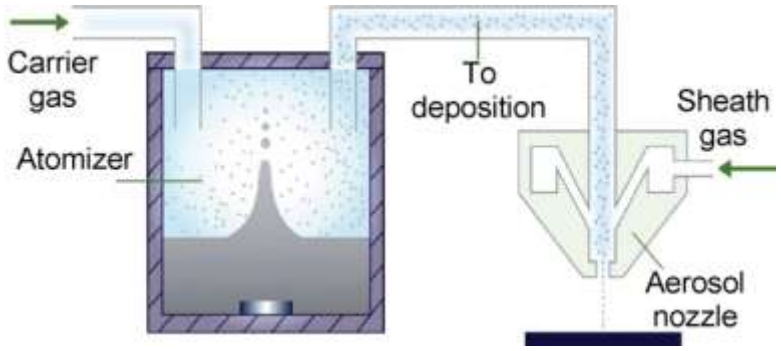

Figure 2: Schematic diagram of the Aerosol-Jet direct write system [9]

1.2.2 Laser Based Processes

Laser based direct write methods use laser energy to transfer or deposit material from solid, liquid or gaseous precursors to form 3D structures. These include laser chemical vapor deposition (LCVD), laser enhanced electroless plating (LEEP), laser enhanced or activated electroplating, laser induced forward transfer (LIFT), laser induced backward transfer and matrix assisted pulsed laser (MAPLE DW). LCVD uses a gaseous precursor and the heat produced by the laser selectively transforms precursor gases to solid material. LEEP uses a liquid precursor and the heat produced by the laser leads to decomposition of the liquid and material deposition. Laser enhanced or activated electroplating uses the heat produced by the laser scanning to accelerate material deposition during electroplating as displayed in Figure 3(a). LIFT uses lasers to transfer a thin film of material from an optically transparent disk coated with material onto a substrate. Laser induced backward transfer, shown in Figure 3(b) uses a laser to vaporize material and deposit it onto an optically transparent surface. MAPLE is similar to LIFT but it uses a carrier material to absorb the thermal shock without thermally affecting the deposition.

Laser processes are accurate, highly repeatable and may not need any further post processing. Certain laser based DW processes, such as MAPLE DW or other similar forward transfer techniques, can also be used with subtractive laser micromachining [11, 12]. Figure 4 shows a schematic of a laser based DW system that can be used for both additive as well as subtractive DW.

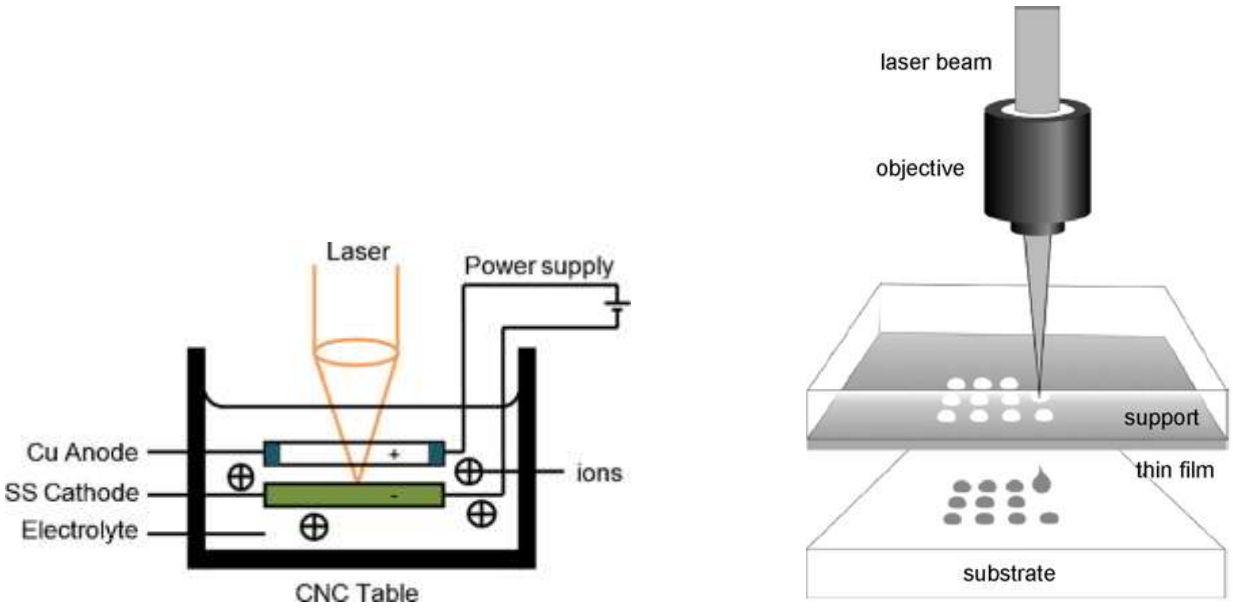

(a) (b)

Figure 3: (a) Laser activated electroplating; (b) Laser induced forward transfer (LIFT) [9]

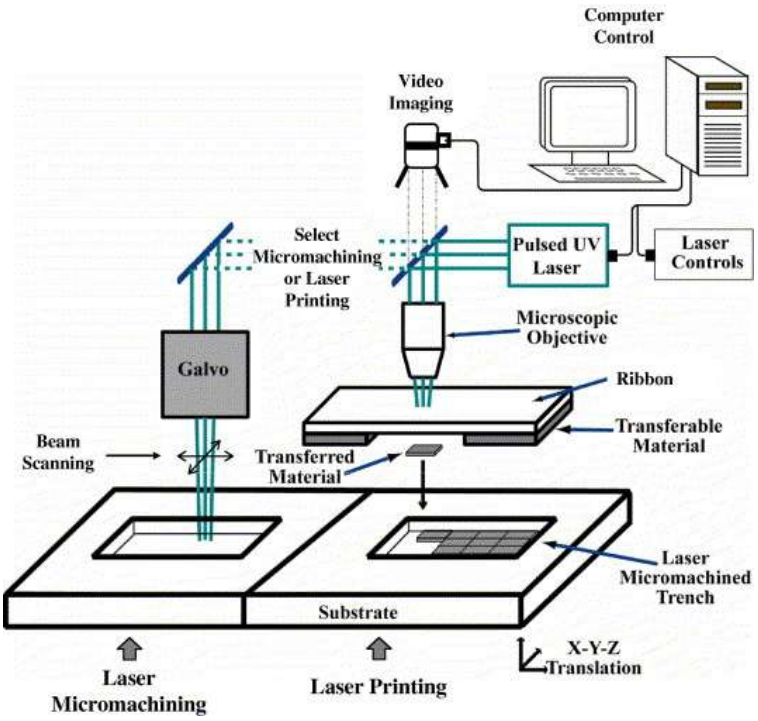

Figure 4: A laser based DW system used in both additive (right) and subtractive (left) modes [12]

1.2.3 Focused Ion Beam and Electron Beam CVD

Focused ion beam (FIB) direct write or FIB CVD and electron beam CVD both operate in a manner similar to laser CVD. An energy beam focused using an electrostatic lenses scans over a substrate in the presence of a gaseous precursor, thus depositing solid material onto the substrate. FIB CVD utilizes a beam of gallium ions generated from a liquid gallium source whereas electron beam CVD uses a beam of electrons. Electron beam CVD is slower that FIB and laser CVD, but FIB and electron CVD offers better resolution at the cost of a lower deposition rate as compared to laser CVD [2, 9]. If used directly on a substrate, a focused ion beam causes sputtering and removal of atoms, and hence finds applications in micro/nano machining as well [2].

1.2.4 Flow Based Processes

Flow-based direct write processes are characterized by technologies where a continuous flow of ink occurs when printing. This is unlike inkjet printing or Aerosol-Jet systems where individual droplets are deposited. Flow-based direct write systems involve pushing an ink through an orifice or nozzle onto a substrate. A commonly used mechanism to push inks is a syringe and plunger arrangement where the

plunger is activated using pneumatics or a mechanical push rod. They use 3-axes of motion control similar to CNC machining to manipulate the nozzle in order to deposit three dimensional structures. A pump-like system developed by nScrypt, which is based on Sciperio's Micro-Dispense Direct Write (MDDW) technology, uses a micro-dispensing pump and a syringe mechanism with precise air pressure control to accurately deposit material. A system developed by nScrypt, called the Micro Mixer pump, allows the user to mix up to three materials on the fly, thus producing engineered structures with locally controlled mechanical or chemical properties. The MicroPen developed by OhmCraft is based on a micro-capillary tip which uses a syringe and pneumatic ram to extrude material through the micro-capillary writing tip. Both of these technologies can be used to print on flat as well as conformal surfaces.

1.2.5 Tip Based Processes

These processes deposit inks using mechanisms similar to that of quills or pens. When a pen tip with ink adhering to its surface is placed near a substrate, ink transfers from the tip to the substrate. Dip-pen nanolithography (DPN), shown in Figure 5, works by dipping an atomic force microscope (AFM) tip into an ink well. The specially formulated ink adheres to the AFM tip and is then used to write a pattern onto a substrate. An array of such tips can also be used to deposit material simultaneously to increase the throughput. Another tip based DW process known as a nanofountain pen (NFP), as shown in Figure 6, is similar to the AFM tip DW process. However, it uses a nano-pipette instead of an AFM tip. A pipette is filled with the ink solution and flows when the tip is brought in contact with the substrate. Tip based processes have been used to deposit proteins, polymers, other bio materials, etc.

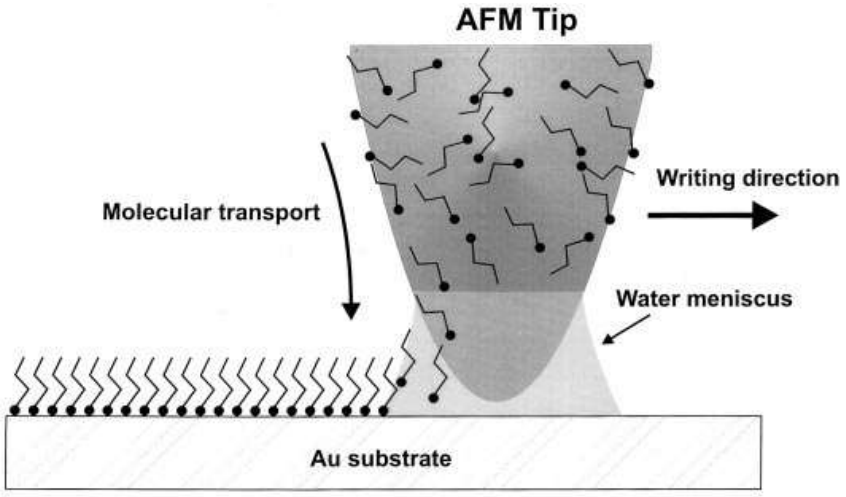

Figure 5: Material deposition using DPN [11]

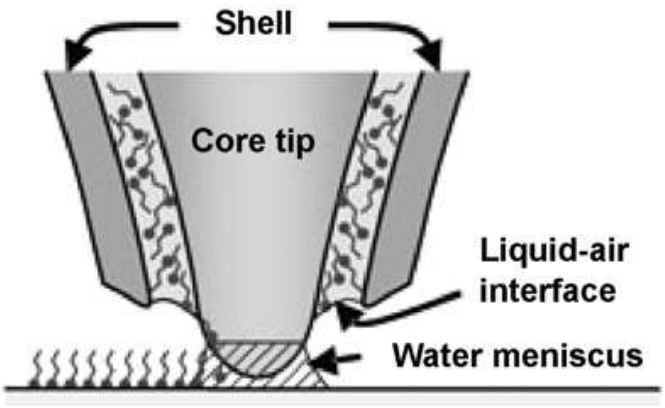

Figure 6: Material deposition using NFP [9]

1.2.6 Materials in DW

Direct write processes utilize high grade starting materials. These inks, slurries or pastes may contain powders, flakes, binders, organic precursors, vehicles, solvents, dispersants, or surfactants to produce customized chemical and rheological properties [9]. As long as the materials that need to be deposited are compatible with the substrate and can be bonded to be substrate with post-post processing techniques (if required), they can be used in direct write. Materials that can be processed using DW include metals, ceramics and salts. Inks and pastes made from powders are most common. Nano-powders are also used but require special safety considerations due to health hazards and high surface energy of powder particles.

1.2.7 Applications of DW

Due to their ability to produce parts of various sizes from nano to meso scale, and due to the wide range of materials that can be printed, direct write techniques can be adapted to a variety of applications such as microelectronics, MEMS, pharmaceutics, biomedical and tissue engineering, to name a few. Processes such as inkjet DW, LCVD and LIFT are well established for micro-optics applications [9]. Wanke et al. [13] used LCVD to deposit aluminum oxide 3D structures to totally reflect certain bands in the electromagnetic spectrum to form mirrors. MAPLE DW has been used to deposit fractal antennas on non-conformal bio-substrates, the abdomen of honeybees to be precise [2, 10]. Due to speed limitation of the laser, only partial antennas were printed on the live specimen. However, a complete antenna was printed on a dead honeybee. Figure 7 shows a printed a printed antenna on the abdomen of the dead honeybee [2]. Inkjet and nScrypt printing methods have also been used to write fractal antennas on living creatures.

Tong et al. used a combination of thermal spraying (additive DW) and ultrafast laser micromachining (subtractive DW) to fabricate embedded microheater structures [14].

Figure 7: A 35GHz fractal antenna printed on the abdomen of a dead honeybee using MAPLE DW [2]

1.3 nScrypt

nScrypt, Inc. formed in 2002, developed a direct write system based on Sciperio's Micro-dispense Direct-Write (MDDW) technology through the DARPA (US Government Defense Advanced Research Projects Agency) MICE program (Mesoscopic Integrated Conformal Electronics). The nScrypt tabletop material dispensing system uses a syringe based high precision extrusion pump to dispense inks or pastes. It uses precision slides to accurately manipulate motion in the X, Y and Z directions in a reproducible manner. The SmartPump is a device that uses air pressure at the syringe end and a valve mechanism near the nozzle to precisely control the amount of material dispensed. Figure 8 provides a schematic of the valve mechanism in a SmartPump. It is available in two sizes, 20 pico-liters and 100 pico-liters. An nScrypt system incorporating a precision Z stage with a height sensor has the ability to print on non-conformal surfaces. The height sensor scans the surface of the substrate prior to deposition and then adjusts machine code in order to follow the non-conformities in the surface. It is a time-pressure dependent system in which the amount of material dispensed is directly proportional to the duration and amount of the applied pressure. The process is controlled by motion control software which allows the user to control the following process parameters – air pressure, valve opening, valve opening and closing speeds, feed rate, motion delays, and dispensing height. A conical ceramic nozzle tip attached to the pump controls the shape of the extrudate. These conical nozzles, developed by nScrypt Inc., are optimized to dispense highly viscous materials, as the pressure required to extrude material through these conical nozzles is

greatly reduced as compared to traditional tubular nozzles [15, 16]. Nozzle tips are available in various orifice sizes from 12.5 to 125 microns inner diameter. Precisely controlled parameters allow the system to produce a negative pressure inside the valve body when the machine is ordered to stop printing. This causes a phenomenon nScrypt terms as "self-aspirating" or "suck-back" [15], that sucks the ink back into the nozzle to reduce material build up at the tip of the nozzle over time. This phenomenon is used to overcome the drawback with other such dispensing systems which are prone to material build up at the nozzle tip over time, reducing their accuracy in placement and dispensing [15]. nScrypt also produces a micro mixer pump that allows the user to print up to three materials simultaneously in order to vary the ratios of the three materials being deposited. This is done by controlling individual air pressures and valve openings. The SmartPump is capable of dispensing liquids with viscosities ranging from 1 up to 1,000,000 cP [15]. Chen et al. [17] used a silver paste, of about 275,000 cP, to pattern high aspect ratio conducting grid lines on silicon solar cells. Upon investigation, it was observed that the high aspect ratio and fine printed lines promote conductivity and reduce impedance. The overall efficiency of the cell is increased by 0.5% as compared to screen printed cells.

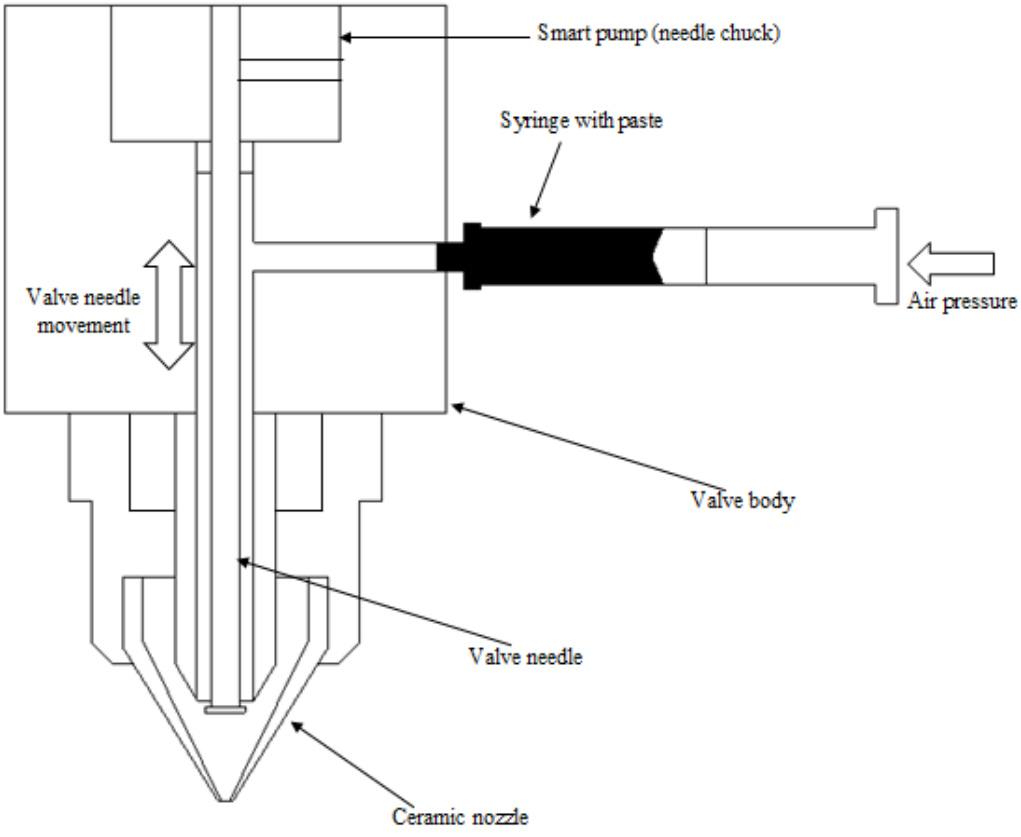

Figure 8: SmartPump schematic

Due to its ability to handle a wide range in viscosities, the nScrypt material dispensing system prints most materials as long as they can be converted into a paste and provided the diameter of the largest particles in the paste are less than the inner diameter of the nozzle used [18]. Li et al. [15] have used this system to print solder paste with a viscosity of 30000cP, as well as a silver particle loaded conductive ink, resistive inks, and polycaprolactone (PCL) dissolved in acetic acid as a bio-scaffold material for tissue engineering applications. Blackburn et al. [18] used ceramic powders such as gadolinia-doped ceria (GDC), yittria-stabilized zirconia (YSZ), LSM and LSCF, from solid oxide fuel cell and gas sensor applications with particle sizes from 150 to 750 nm. Pastes were prepared by mixing them with binder vehicles. These mixtures were prepared using a Thinky centrifugal mixer. Pastes with high solids loading were produced by mixing the powders with a water-based solution. Darvan-C was used to disperse the sub-micron particles [18].

Kadara et al. [16] demonstrated volumetric reproducibility of electrochemical platforms using an nScrypt material dispensing tool. The authors compared its performance to those of electrochemical platforms produced using screen printing. A carbon-graphite ink was used to manufacture 3mm diameter circles of 20μm thickness on a polymer substrate, and the tested samples exhibited electrochemical responses and reproducibility comparable to samples manufactured using screen printing [16].

Lopes et al. [19] used a conjunction of stereolithography and the nScrypt SmartPump 100pL to fabricate 2D and 3D embedded electronic circuits as an alternative to conventional PCB manufacturing. Conventional techniques limit the PCB to a planar design and increased space requirements. Li et al. [15] implemented the precise control of the SmartPump's pumping technology to print an array of 1000 dots, with only a 10% variation in dot size, to demonstrate applications in the electronics and MEMS industry.

As discussed above, existing research on nScrypt material dispensing systems has primarily been focused on replacing conventional material deposition processes with nScrypt's maskless non-contact printing technique, especially in the printed electronics field. Li et al. [15] have done some preliminary research on the effects of dispensing height or tip standoff on the flow rate of material exiting the nozzle. Figure 9 is a graphical representation of the effect of dispensing height and pressure on the flow rate as studied by Li et al. [15].

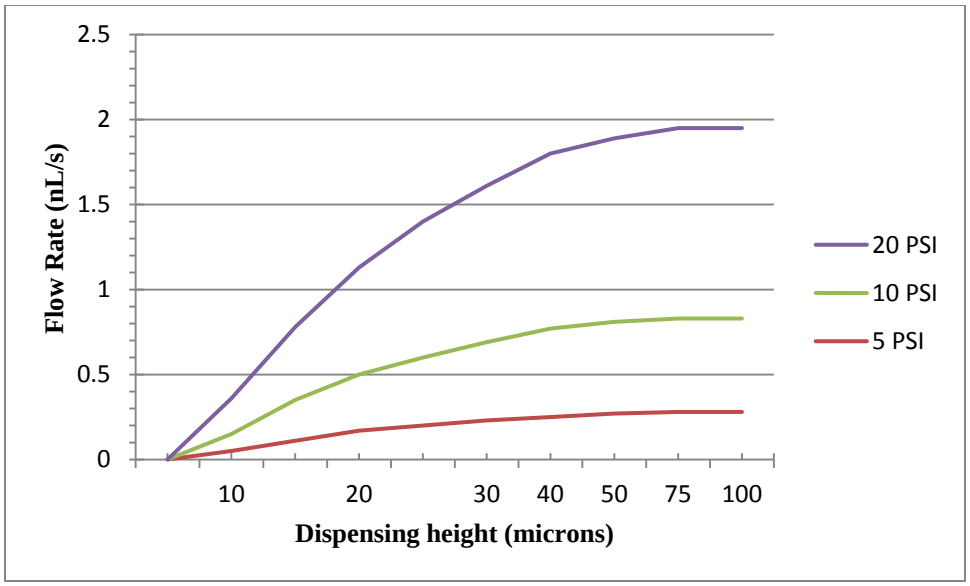

Figure 9: Flowrate vs. dispensing height [15]

1.3.1 Operating Mechanism

The nScrypt tabletop dispensing system uses a three axis motion platform with X and Y stages to move the work table, and a Z stage to move the deposition head. The deposition head, or SmartPump employs a needle valve type mechanism that very accurately controls material flow using air pressure and valve position control. The valve body holds the ceramic nozzle through which the ink is extruded and deposited onto a substrate. An ink or paste is made and is drawn into a 3cc plastic syringe barrel. The syringe is then attached to the valve body using a 10-32 luer adapter. Figure 8 shows a schematic of a SmartPump with a syringe connected to the valve body. A source of pressurized air is connected to the rear side of the syringe. Air pressure is then applied to the syringe, and the ink or paste flows into the valve body. When the valve rod is moved down, the hermetic seal between the valve rod and valve body is opened. Ink then flows into the nozzle. Figure 10 shows the operating mechanism of a SmartPump in the three steps described above. When the pressure crosses a certain threshold level for a given ink's rheological properties, ink flows out of the nozzle. By manipulating movement of the X, Y and Z, stages three dimensional structures can be built layer by layer. When the valve rod moves back up, the valve closes and the flow of ink stops. This upward movement of the valve rod produces a small negative pressure within the valve body which sucks the ink at the tip of the nozzle back up into the chamber. This keeps the nozzle tip clean, reduces material buildup at the tip, and provides precise control over material flow at the start and stop of a print cycle.

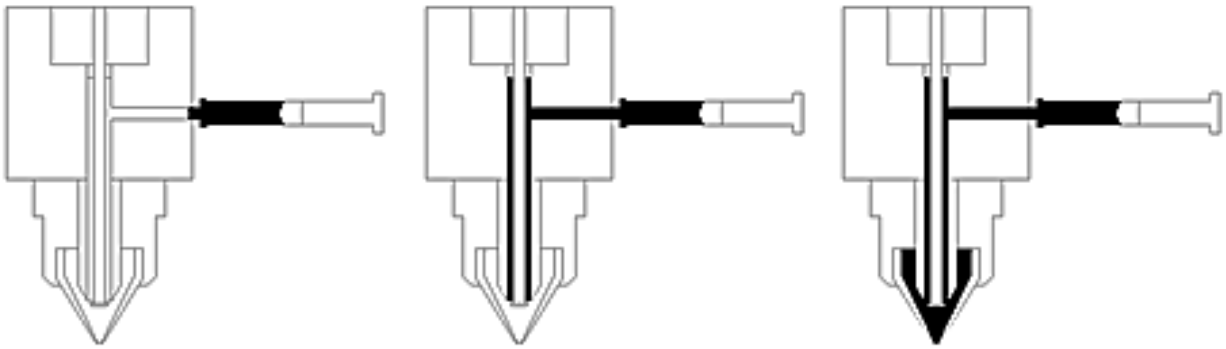

(a) (b) (c)

Figure 10: Functioning of the SmartPump; (a) syringe with paste attached to the assembled valve body; (b) air pressure applied to the syringe; (c) when air pressure is applied and valve is opened.

All machine parameters are controlled by software provided by nScrypt. The air pressure and print home or job home (starting X, Y and Z, meaning starting standoff) are controlled by the software. Other parameters, namely feed rate, valve positions, valve opening and closing speeds, and feed rate (tool manipulation in X, Y and Z) are controlled using a script file in text format (*.TXT). A sample machine code used in the experiments is given in Appendix A.

1.4 Problem Statement

Process parameter values used with the nScrypt tool will dictate dimensional properties of print tracks. Depending on the application, one might need to control the height and/or width of a track. For example, large area fill patterns may require wide tracks with controlled layer thickness, whereas applications requiring a large number of features packed in a small area may require narrow print tracks that are tall enough to provide a sufficient cross-section for applications requiring high electric/ionic conductivity. A large part of the research conducted on the nScrypt SmartPump deals with its application to fields such as printed electronics, MEMS, sensors etc. Blackburn et al. [20] conducted two experiments to plot the effects of feed rate and air pressure in the thickness and width of printed lines. Li et al. [15] conducted an experiment to measure the effects of standoff distance and air pressure on the volumetric flow rate of paste through the nozzle tip. However, research that quantitatively measures the effects of paste viscosity

or solid loading fraction on the dimensions of printed lines is lacking. Also, a single process model incorporating all the user controlled process parameters has not yet been presented in literature. The primary goal of this thesis is to develop such a process model.

1.4.1 User Controlled Process Parameters

The nScrypt material dispensing system is based on a micro-extrusion process, and the output feature size is controlled by varying user controlled input parameters fed into the system. Controllable parameters of the nScrypt system with the SmartPump tool attachment are as follows.

1. Valve position – the position of the valve needle when valve is opened, influences the flow rate of the ink exiting the valve body and entering the nozzle.
2. Standoff distance – the distance between the nozzle tip and the printing substrate, measured in 'mm'. This influences the shape of the track.
3. Air pressure – applied at the back end of the syringe that contains the ink or paste that the system needs to extrude. Air pressure influences the flow rate of the ink and is measured in PSI
4. Valve opening speed – the speed at which the valve needle translates, in mm/sec, when the valve is opened. It influences the flow of the material at the start of the print cycle.
5. Feed rate – travel speed, in mm/sec, of the nozzle during printing controls the amount of ink deposited per unit length, and affects the width and continuity of the bead.
6. Motion delay – the time for which the nozzle waits at the point where the needle valve is opened to allow initial flow of material and to obtain a uniform bead width over the entire bead. It is measured in seconds.
7. Nozzle diameter – diameter of the nozzle opening in μm. It affects the flow rate of the ink and the diameter of the extruded track.
8. Ink viscosity – this property of the ink affects the flow of the ink throughout the print cycle.

Some effects of individual parameters or a combination of parameters on the dimensional properties of a printed line are discussed in Table 1.

Table 1: Possible outcomes of printing

Bead	**Description**	**Possible Causes**
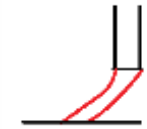 or 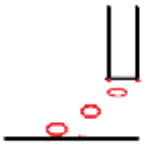	Narrow track Or Track breaks off into individual droplets	Standoff distance too large. Feed rate too high. Motion delay too small. Valve open speed too low. Ink viscosity too high or too low for used settings.
	Mushrooming	Air pressure too high. Nozzle too close to substrate – standoff distance too small. Feed rate too low. Motion delay too long.
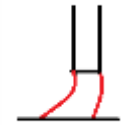	Just right	

In order to accurately print a designed structure, it is imperative to be able precisely predict process output based on machine input parameters. Hence, a statistical model that relates the input parameters of the nScrypt micro-extrusion process to the dimensional properties of the output of this micro-extrusion process is required.

1.5 Thesis Objectives

As discussed previously, this thesis aims to fill the knowledge gap left by the lack of a method to accurately predict the process output of an nScrypt SmartPump by investigating the effects of changing process parameters on process output. The primary objectives of this thesis are to study the process parameters of the nScrypt tool and to develop a mathematical relationship between process input parameters and resulting dimensional properties of printed features using particulate suspension paste.

Chapter 2

Literature Review & Research Methodology

2.1 Literature Review

2.1.1 Robocasting

Traditional additive manufacturing techniques for processing ceramics, such as 3D printing onto ceramic beds, produce porous parts. Several techniques have been used to produce dense ceramic parts such as fused deposition of ceramics (FDC), laminated object manufacturing (LOM) with ceramic loaded tapes, modified stereolithography (STL) with ceramic loaded UV-curable resins and extrusion techniques using organic solvent based particulate slurries. These techniques require binder burnout prior to sintering. Sandia National Labs developed a technique called robocasting which is a slurry or paste extrusion based additive manufacturing process similar to nScrypt's SmartPump technology. Robocasting employs aqueous particulate slurries not requiring organic binders. Since binder burnout is not required, parts can be printed, dried and sintered within 24 hours [21, 22]. The slurries used in this process are highly loaded with ceramic powder (50-65% by volume) and have 35-50 vol.% volatile solvent (usually water) with less than 1 vol.% organic additives or dispersants [21, 22]. Computer controlled robotics are used to deposit these ceramic slurries through an orifice. The size of the orifice can range from as small as 200 μm to as large as 2 mm [21]. The slurries are developed such that they are pseudoplastic enough to flow through the orifice. However, the solvent needs to be volatile enough to stop the mass from flowing after deposition. This allows accurate shape reproduction and gives the user the ability to stack layers and build structures with high aspect ratios. Robocasting equipment has the ability to print on flat or curved surfaces made from plastics, ceramics or metals [23]. As the material is extruded, the orifice motion relative to the substrate, coupled with the given flow rate of material at the orifice, produces the required diameter of the extruded bead. A mixing head developed for robocasting, at Sandia National Labs, has the ability to deposit up to four different materials at once. The mixing system uses a rotating paddle in a small mixing chamber just before the orifice to uniformly mix the materials before deposition [21]. Cesarano et al. [21, 22] have printed functionally graded materials (ceramics and metals) [24], and three dimensional structures using fugitive materials to demonstrate the capabilities of this mixing head.

Denham et al. [25] studied the mechanical behavior of robocast alumina. They concluded that the densities exhibited by robocast samples were comparable to alumina processed by traditional techniques such as slip casting and pressing. However, the mechanical strength of robocast alumina was dependent on the tool paths used to build the test samples. Strengths of robocast samples along the print direction were comparable to the slip cast samples. Whereas strengths of robocast samples perpendicular to the direction of print were less than slip cast samples, but higher than that of the pressed samples. Russias et al. [26] employed robocasting to fabricate porous hybrid organic/inorganic biocompatible scaffolds. The inorganic components were either hydroxyapatite powders or high-silica bioactive glass, and their inclusion increased the stiffness of the scaffold without making the scaffold brittle. Scaffolds with up to 70 wt.% ceramic content could also be machined. The organic content of the scaffolds used were two Food and Drug Administration (FDA) approved bioresonable polymers for medical applications, namely poly lactic acid (PLA or polylactide) and polycaprolactone (PCL) [27, 28].

2.1.2 Process Parameter Modeling

Process parameter settings can greatly influence the productivity, quality, and costs of production for a given process. Determining optimal process parameter values is beneficial in any industry. Trial-and-error and Taguchi's parameter design methods have commonly been used as tools for determining optimal process parameters [29]. Taguchi's parameter design technique is a variation of the classical design of experiments concept. Oktem et al. [30] applied the Taguchi optimization technique to reduce warping in thin-shell plastic injection molding parts. They used MoldFlow to generate data from different combinations of process parameters based on a three level orthogonal Taguchi design and analyzed the data using signal-to-noise and analysis of variance (ANOVA) to determine the effects of process parameter on warpage and shrinkage.

Deng et al. [31] explain that using a trial-and-error process can be costly and time consuming. Moreover, it is impossible to verify the actual optimal process parameter settings using the trial and error method. And although Taguchi's parameter design method offers orthogonal and robust designs, one can only find the optimal output levels using discrete values of parameter levels and level combinations that are specified in the design [29, 31, 32]. Hence Taguchi's approach becomes unsuitable when one of the process parameter variables is continuous. Furthermore, when engineers deal with a multi-response process parameter design problem, the conventional Taguchi parameter design method runs into difficulties [32].

Linear regression and linear programming are widely used techniques for solving optimization problems [29]. This method basically expresses the response or dependent variable as a linear function of process parameters or independent variables where the terms of the function, parameters, and unknown constants are linear. Deng et al. [31] used a combination of Taguchi's parameter design method, regression analysis and the Davidon-Fletcher-Powell (DFP) method to determine optimal process parameter settings of injection molding. They used a three phase process where the first step was to use Taguchi's parameter design method to obtain an initial optimal solution. This is followed by regression analysis to build a prediction model where the target response variable is expressed as a dependent variable in terms of the controllable process parameters (the independent variables). In the third phase, the DPF method was applied so that the target value for the response variable was used to search for the final optimal process parameter settings.

When using experimental design, it is critical to decrease the number of runs in the study. This helps reduce the amount of time required with the machine, and it limits the use of material resources as well [33, 34]. To reduce the number of runs, high-order interactions are assumed to be negligible so that the information for main effects and low-order interactions can be obtained from a fraction of the experimental runs of a full factorial experiment [34]. This is done by confounding main effects and low-order interactions with high-order interactions. Designs where main effects are confounded with three-factor interactions and designs where two-factor interactions are confounded with two-factor interactions are called Resolution IV designs. Resolution IV designs allow the experimenter to estimate all the main effects and some of the two-factor interaction effects. Resolution IV or better designs are ideally preferred [35].

2.2 Methodology

For this work, all experiments have been conducted using an nScrypt Tabletop Material Dispensing System with the SmartPumpTM tool. The ink formulation and printing conditions are further detailed as follows.

2.2.1 Ink Preparation

All experiments were carried out using NiO-YSZ (a mixture of Nickel Oxide and Yttria-stabilized Zirconia) based ink. NiO-YSZ is a typical anode material in a YSZ based solid oxide fuel cell (SOFC). The ink was formulated using tape-casting grade NiO-YSZ powder and Ink Vehicle, both used as

purchased from Fuel Cell Materials (www.fuelcellmaterials.com). Predetermined quantities of powder and ink vehicle were measured and transferred to a 35ml mixing cup. A homogenous paste was prepared using a Thinky ARE-310 planetary centrifugal mixer. The ink vehicle uses a low vapor pressure terpineol solvent. The spinning of the ink in a centrifugal mixer causes the mixture to heat up. To avoid solvent loss, a mixing cycle with pauses in between steps was followed to allow for cooling of the mixture. Figure 11 shows a graphical representation of the mixing cycle. Once mixed, paste was transferred to a 3cc syringe and used for printing.

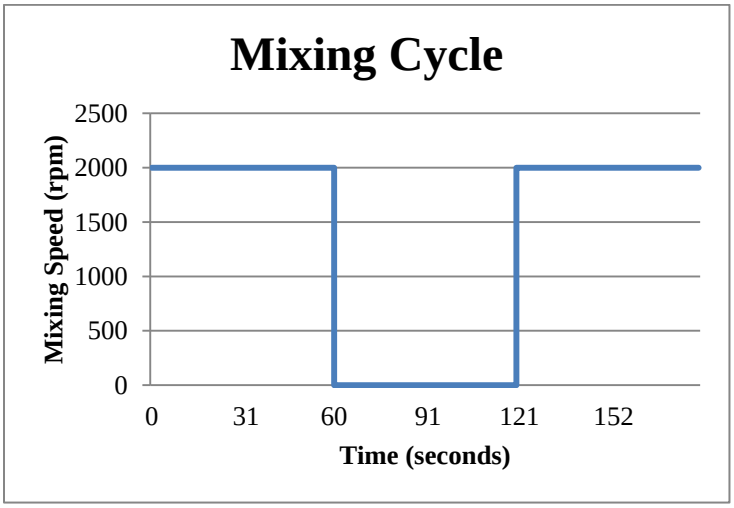

Figure 11: Mixing cycle program for the Thinky mixer

Since materials used for paste preparation have a high cost, and a large quantities of paste are required for accurate and repeatable viscosity measurements, the solid loading fraction of the paste was used in place of viscosity, viz. the ratio of the mass of powder (in grams) to the volume of ink vehicle (in ml).

2.2.2 Printing

The 3cc syringe, once filled with paste, was connected to the valve body in an nScrypt SmartPump dispensing system using a luer to 10-32 adapter. An air pressure line was connected to the rear end of the syringe. The valve rod was moved to its open position, and pressure was turned ON. Once the paste started flowing and equilibrium was reached, the valve was closed. A 3”x4” sheet of Mylar was cut and placed on the vacuum platen of the nScrypt machine. The vacuum pump was turned on to securely hold the substrate down during printing. The printing surfaces were cleaned using 2-propanol before printing. The nozzle tip was then brought to the desired printing location. Once all parameter were set to the

experimental value and equilibrium was reached, the script file was loaded and executed. The printed lines were then allowed to air-dry for 24 hours before being transferred to the measuring apparatus.

2.2.3 Measurement

Two different measuring instruments were used to conduct the measuring part of the experiment.

1. Hirox KH 7700 digital microscope

   Printed samples were placed on a white background under the microscope to provide adequate contrast. The microscope was focused on the bottom layer of the printed line, and line width was measured from edge to edge of the printed line using parallel measure bars.

2. Keyence IL-030 laser profilometer

   The IL-030 laser sensor was used in conjunction with an amplifier unit, IL-1000 and a serial communication unit, DL-RS1A. The communication unit was set up using a mechanical relay and a function generator such that it sent six data points every second. The substrate was translated at 30µm/sec. The effective sampling rate of the system became one data point every 5µm. Printed samples were placed on the nScrypt platen, and the laser profilometer was zeroed on the surface of the Mylar sheet. The output from the communication unit was stored in an MS Excel spreadsheet. Height was calculated as the average of five data points farthest from zero.

Chapter 3

Experimental Results and Discussion

3.1 Preliminary Experiments

Initial experiments were conducted to test the feasibility of fitting a regression model to predict process output as a function of parameter settings. It was hypothesized that the following effects would result from changes in input parameters:

1. Air pressure should control the mass flow rate, i.e. amount of material being pushed out of the nozzle tip. Higher pressures should translate to higher mass flow rates.
2. Higher viscosities (solid loading fractions) make it difficult for the ink to flow. Thus higher air pressures should be required to extrude highly viscous pastes.
3. Lower viscosity (solid loading fraction) allows the ink to flow more easily. This would cause the ink to flow laterally after it has been deposited. Hence the resulting line width should be wider than what was initially deposited.
4. The amount of material deposited should be inversely proportional to the feed rate. At lower speeds more material is deposited, whereas at excessively high speeds too little material will be deposited per unit travel. In this case the printed track should break up into small beads.
5. Standoff distance affects the flow rates of ink extruded through the nozzle. If the nozzle is too close to the substrate, there should not be enough room for the ink to flow and material flow should be reduced. If the nozzle is too high up from the substrate, beads of paste flowing out of the nozzle will break up due to surface tension and the printed track will not be continuous [15].
6. Ease of flow also depends upon the nozzle size. Smaller nozzles should require lower viscosities and/or higher pressures.
7. Motion delay and valve opening/closing speed affect the quality of the beginning or end of the printed line. A large value for motion delay or a high valve opening speed should cause excessive material deposition at the start of a line.
8. High pressure and low standoff distance will cause excessive material to flow laterally out of the nozzle and cause a mushrooming effect as shown in

9. Table 1. Excessive material will stick to the nozzle and will distort the printed line and will drag material in the direction of the feed causing non-uniform printing.

3.1.1 Paste Properties

Paste rheology strongly influences its behavior within the system and post extrusion as well as dimensional properties following extrusion. To understand some of the properties of the pastes used in the experiments, a Brookfield DE-V viscometer was used to measure the viscosity of the ink vehicle at different shear rates produced when spindle speed is varied. Figure 12 displays the viscosity profile of ink vehicle. A minor shear thinning behavior was observed in the ink vehicle which is beneficial in an extrusion process. To check its behavior when the ink vehicle is loaded with solid particles, a paste of NiO-YSZ and ink vehicle with a solid loading fraction of 2.4 g/ml was mixed in the Thinky mixer. The same test was repeated. The viscosity profile of the paste is given in Figure 13. It was observed that a significant shear thinning occurred in the paste.

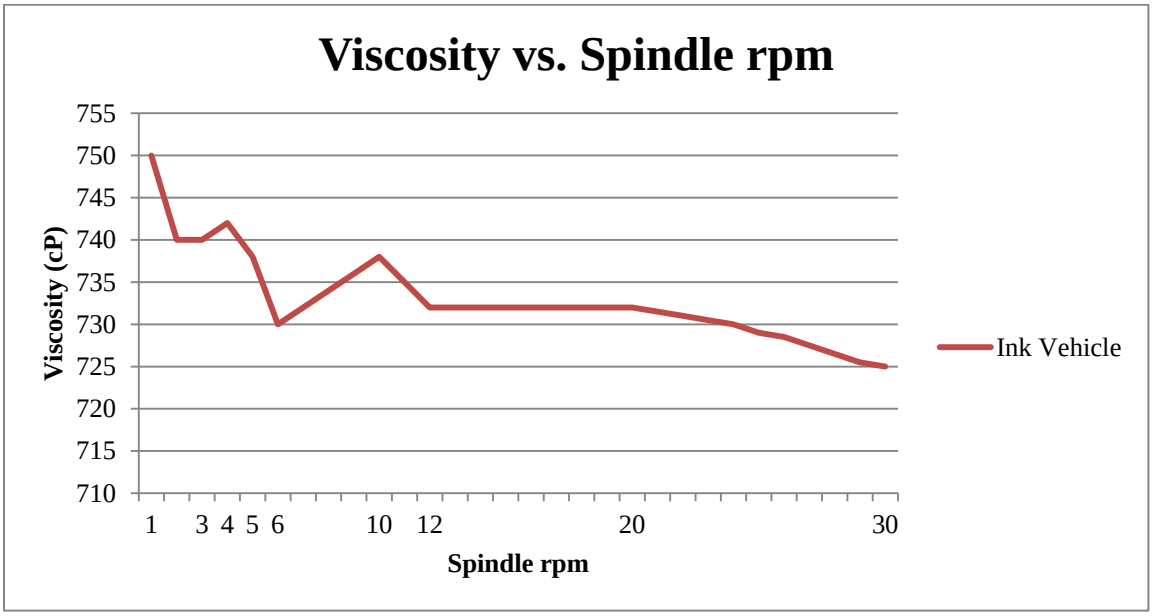

Figure 12: Ink vehicle viscosity vs. spindle rpm

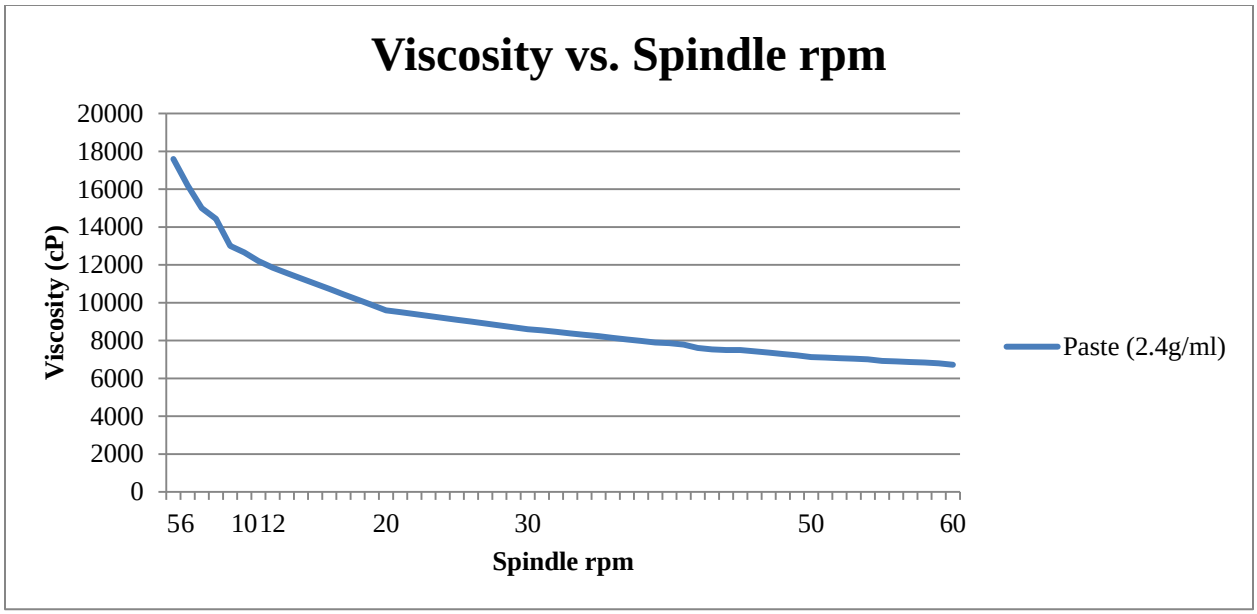

Figure 13: Viscosity vs. shear rate of paste with 24g/ml solid loading

3.1.2 Feasibility Test

For the feasibility test, a simple experiment was conducted by varying only two parameters – nozzle size and pressure. The remaining six input parameters, namely valve position, valve opening speed, feed rate, motion delay, standoff distance and solid loading fraction (viscosity) were kept constant. The response measured in the experiment was the width of the printed line. This was measured using the Hirox digital microscope. The constant parameter settings were:

1. Valve position– 1.8 mm
2. Valve opening speed – 10 mm/sec
3. Feed rate – 5 mm/sec
4. Motion delay (Wait) – 0.1 sec
5. Standoff – 50 µm
6. Solid loading fraction – 5.75 g/ml

Two nozzle sizes were used – 100 µm and 125 µm, and air pressure was varied from 0-42.5 PSI in steps of 2.5 PSI. Three lines were printed for each parameter combination in the experiment, and one width measurement was conducted for each line. The average width response was then calculated and considered as a single replicate for the experiment. Eureqa (http://creativemachines.cornell.edu/eureqa), a

software tool developed at Cornell University for detecting mathematical relationships in data, was used to generate a regression equation to fit the data using mean square error as the error metric.

Table 2: Preliminary experiment data

Pressure (PSI)	Width avg. for 100µm Nozzle (µm)	Width avg. for 125µm Nozzle (µm)
2.5	-	294.26
5	-	315.51
7.5	-	355.96
40	184.79	305.58
12.5	209.23	288.07
15	242.43	323.40
17.5	280.19	294.60
20	300.51	338.99
22.5	345.90	394.24
25	300.52	658.04
27.5	436.53	973.13
30	441.70	813.34
32.5	425.65	758.16
37.5	478.89	775.43
40	571.63	879.08
42.5	552.25	883.88
35	455.65	(Validation Run)

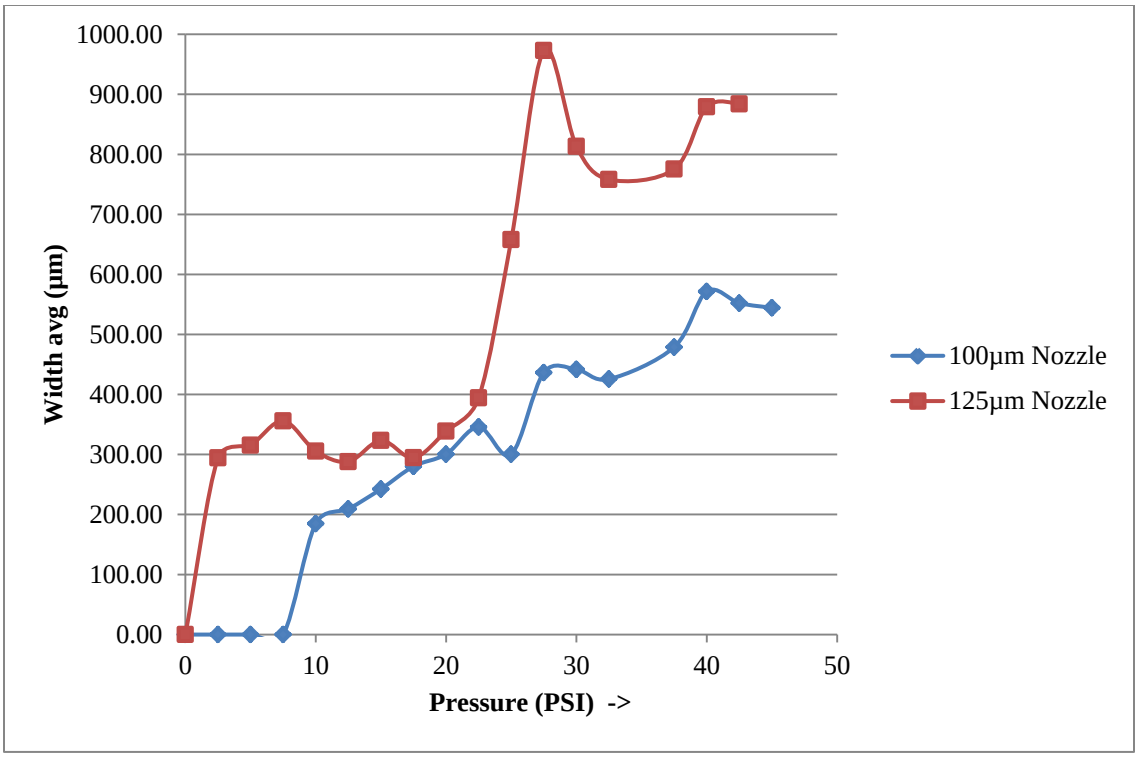

Figure 14: Width vs. pressure

Data from the experiment is tabulated in Table 2. Figure 14 shows a plot of the data obtained from the experiment. Using Eureqa, the width *(y)* of a printed line was defined as a function of the nozzle size *(n)* and air pressure *(x)*.

$$y = f(x,n) = ncos(9.6324396xn) + 15.94794x + 9.6324396n - 1011.5082 \quad \ldots\ldots(1)$$

3.1.3 Validation

To verify the model generated using Eureqa, we use the function to predict the width for parameter setting within the experimental space that were not included in the model. A line was printed at this setting, and its actual width was compared with the predicted width. For this case, process settings considered were – a 100 µm nozzle diameter and 35 PSI air pressure. Predicted width was calculated as 465.295 µm using equation (1) in Eureqa. Figure 15 shows the prediction window from Eureqa.

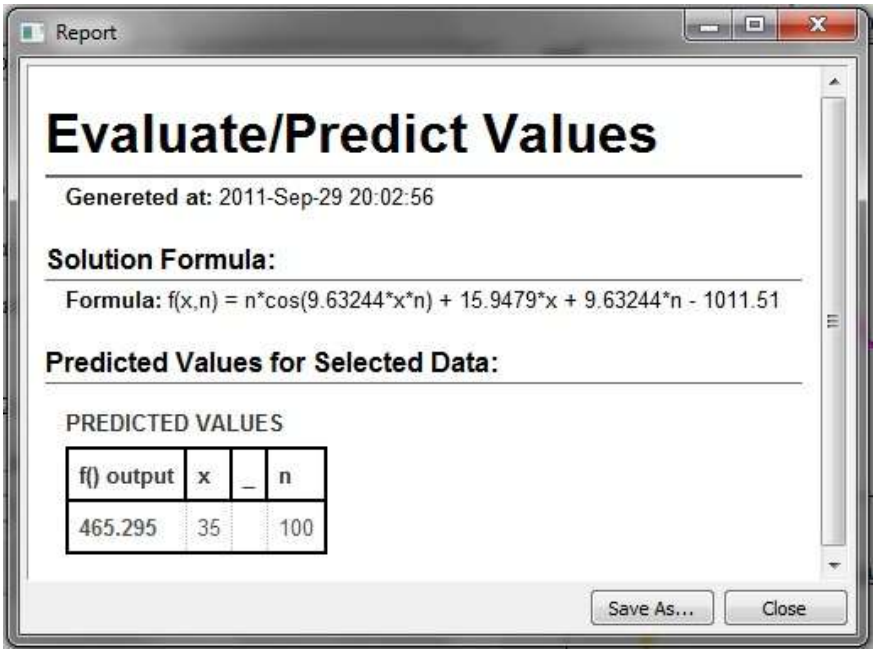

Figure 15: Prediction value using Eureqa

The printed width for these settings was found to be 455.65 µm. In comparison to the predicted value of 465.295 µm, a 2% error was observed. It was concluded that more data than the single replicate used here would help to build a more accurate model and reduce the error further. Also, outliers such as the one observed in Figure 14 with the 125µm nozzle at 27.5PSI air pressure can be analyzed with more data and eliminated if anomalous.

Feasibility Test Discussion

A regression model was successfully fitted to the experimental data, and the observed effects of varying air pressure and nozzle size were consistent with the initial hypothesis. An increase in air pressure leads to increased material flow and increased line width. It was also observed that an increase in nozzle diameter resulted in increased width.

It was observed in the experimental data in Table 2 that with the smaller nozzle diameter at lower pressures, no material was extruded thus giving null data points, viz. process settings where material was not extruded. To avoid such data points in future experiments, it was decided that a lower solid loading fraction would be used for ink formulation.

3.2 Screening Experiment

The first step was a screening experiment carried out to determine the factors that have a significant effect on the response variable. This was done in order to conserve resources and to weed out insignificant factors so that further analysis could be carried out only on the significant factors. For this screening experiment, all eight controllable parameters in the nScrypt micro-extrusion process were taken into consideration. Minitab was used to investigate possible design options for a two level eight factor experiment. Both 2^{8-3} and 2^{8-4} designs have a resolution of IV, which means all the main effects are only confounded with three-way interactions effects or higher. To use the least amount of resources without sacrificing the amount of information gathered from the experiments, a two level fractional factorial 2^{8-4} experiment was selected. Randomization of runs would cause the pressure value to shift between its high and low levels repeatedly throughout the experiment. It has been observed that repeated cycling between low and high air pressure settings causes the formation of air pockets inside the syringe and valve body. This in turn causes non-uniform and interrupted printing. In order to incorporate randomization into the experiment, the entire system would have to be flushed and cleaned after each run, which would take an inordinate amount of time and would require excessive use of cleaning supplies leading to waste of experimental paste materials. Also, two distinct pastes were to be printed, which meant a changeover would also require a system clean up. In the interest of time and resources, the experiment was therefore not randomized. A four replicate experiment was designed to account for some of the random variability in the response variable and these replicates were printed in a single setup without changeovers.

Table 3: Factor levels for screening design

	Factor	Low (-1)	High (+1)
1.	Feed (F)	5 mm/sec	10 mm/sec
2.	Pressure (P)	10 PSI	20 PSI
3.	Nozzle (N)	100 µm	125 µm
4.	Solid loading fraction (V)	2.4 g/ml	4.8 g/ml
5.	Standoff (S)	50 µm	100 µm
6.	Valve position (VP)	1.7 mm	2.5 mm
7.	Valve opening speed (VOS)	5 mm/sec	10 mm/sec
8.	Wait (W)	0.1 sec	0.2 sec

Discussion

Factor levels used in the screening experiment are shown in Table 3. Factor levels for the screening experiment were determined as follows

1. Solid loading fraction – based on the preliminary experiment and to avoid parameter settings where no line is printed, lower solid loading fractions were used
2. Feed rate – based on the preliminary experiment and the fact that lower viscosities were used a higher range of feed rates was selected for the screening experiment
3. Pressure – air pressure levels were selected based on the levels used in the preliminary experiment
4. Nozzle size – nozzle size was selected based on their availability
5. Standoff – the range was based on the preliminary experiment and on the level and range of standoff distances used in the work done by Li et al. [15]
6. Valve opening – was based on the level used in the preliminary experiment and the allowable limits of valve positions given in the system's user manual
7. Valve opening speed – was based on the preliminary experiment level and the maximum allowable speed as given in the system's user manual
8. Wait time – was based on the preliminary experiment

The design table and data from the screening experiments are tabulated in Appendix B.1. The height and width were analyzed as independent responses.

3.2.1 Analysis of Height Data

Minitab was used to analyze the factorial data. The half normal plot for height is shown in Figure 16.

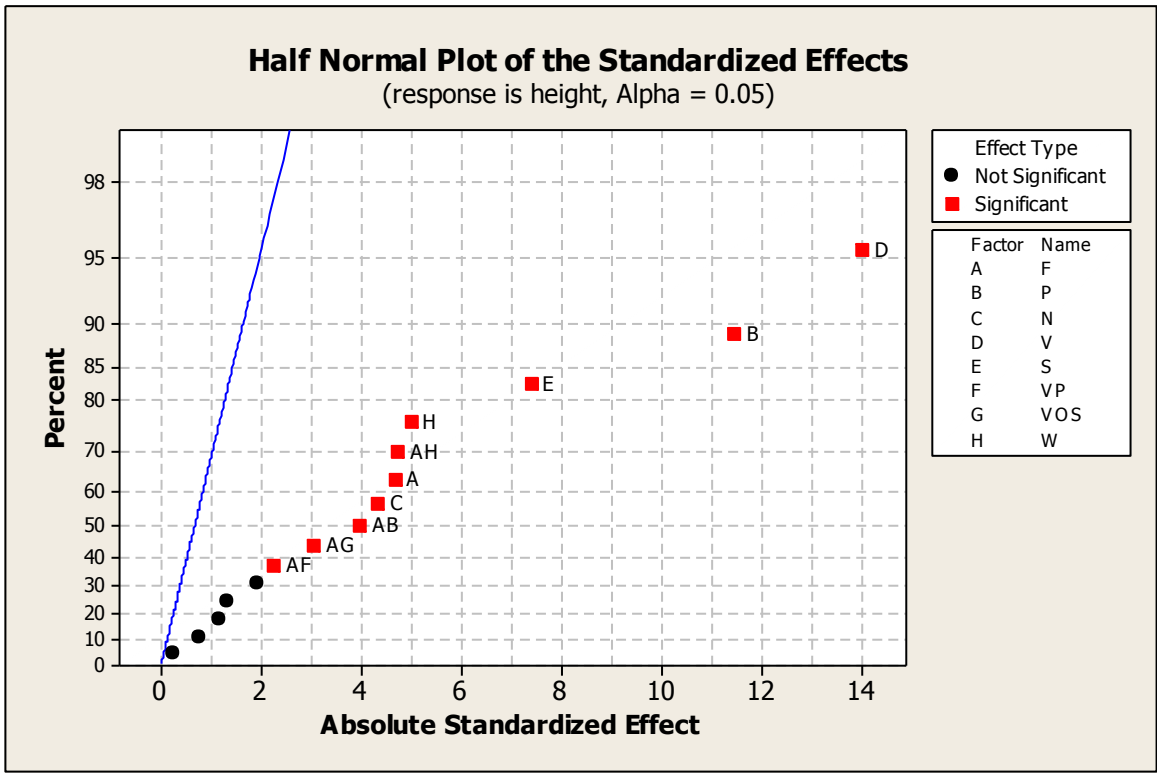

Figure 16: Half normal plot for screening height analysis

From the half normal plot in Figure 16, it was established that factors D (V/solid loading fraction), B (P/pressure) and E (S/standoff) were the most significant. While other factors and interaction terms are shown as significant in the half normal plot, it should be noted that because four replicates of the experiment were executed, the error term is based on those replicates. Since the runs were not randomized, this likely resulted in an artificial low level of experimental error. Using these factors a regression analysis was carried out in Minitab and a regression equation was generated. The residual plots from the regression analysis are shown in Figure 17. A visual inspection of the normal probability plot and histogram revealed normality of residuals. This was verified using a test for normality in Minitab. Figure 18 shows a normal probability plot of the residuals with a goodness of fit test. The p-value obtained was 0.326, hence it was concluded that the residuals were normally distributed. The 'Versus Fits' plot did not indicate abnormalities in the variance, and there was not enough evidence to suspect

non-constant variance. The 'Versus Order' plot did not exhibit any patterns. Hence we accepted the model and proceeded to test the validity of the regression equation.

$$height = 71.6232 + 11.5462P + 14.105V + 7.4483S \quad \ldots\ldots(2)$$

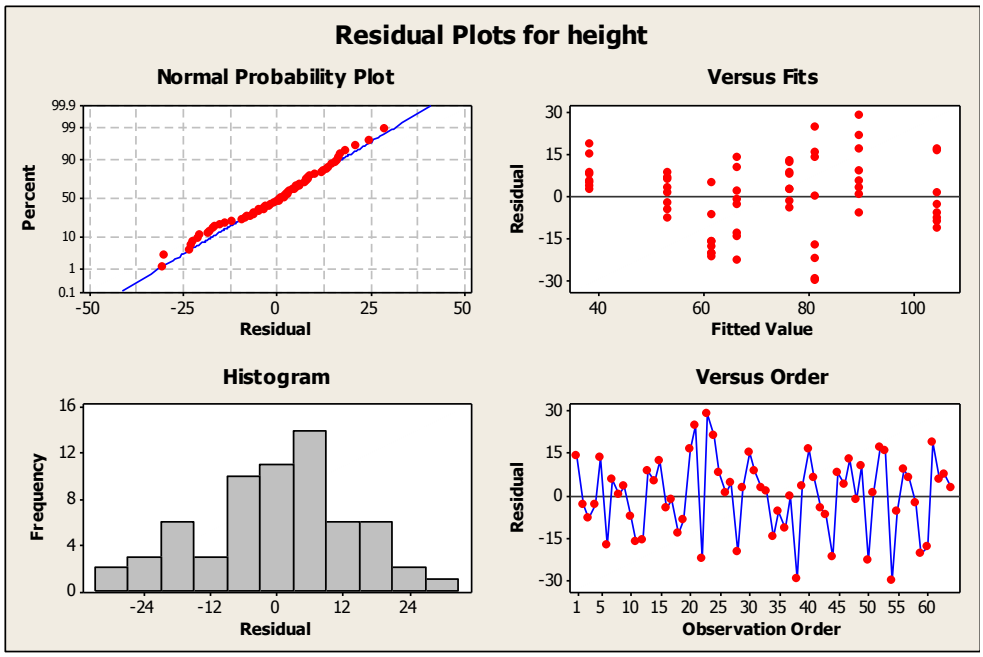

Figure 17: Residual plots of regression analysis of height from screening experiment

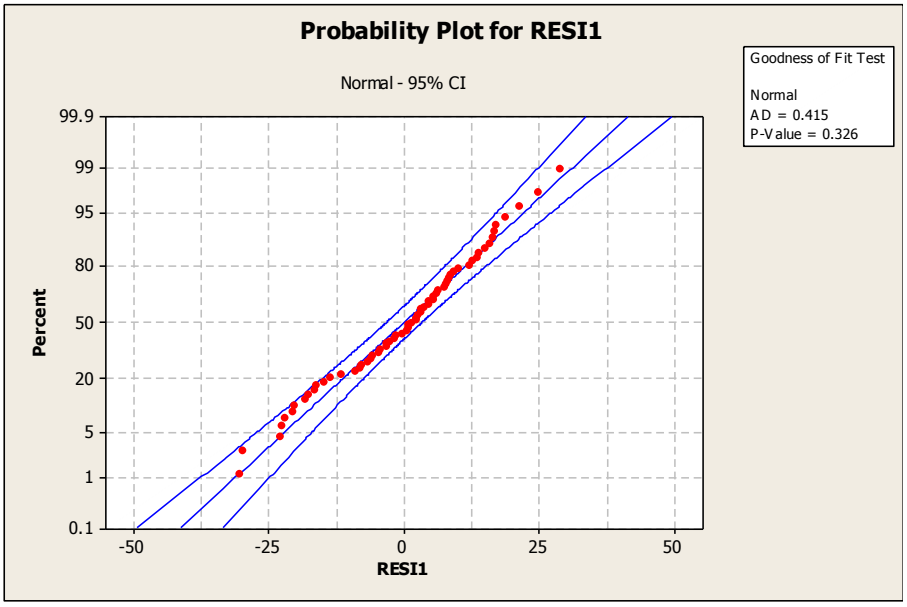

Figure 18: Normality test for residuals from regression analysis of height from screening experiment

3.2.2 Analysis of Width Data

A factorial analysis was carried out on width data using Minitab.

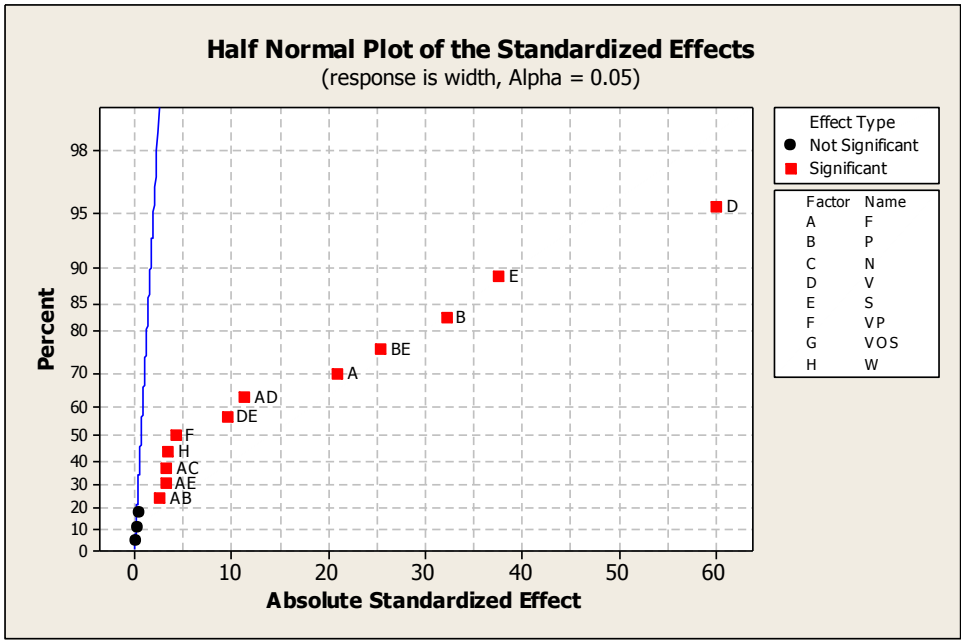

Figure 19: Half normal plot for screening width analysis

From the half normal plot in Figure 19, factors D (V/solid loading fraction), E (S/standoff), B (P/pressure), A (F/feed) and interaction BE (P/pressure*S/standoff) were deemed the most significant. As noted above, an artificially low level of experimental error is suspected. Using these factors, a regression analysis was carried out in Minitab and a regression equation was generated. The residual plots from the regression analysis are shown in Figure 20. A preliminary visual inspection of the normal probability and histogram plots and a test for normality in Minitab were conducted to verify normality of the residuals. Figure 21 shows a normal probability plot of the residuals with a goodness of fit test. The p-value was observed to be 0.476, and it was concluded that residuals for this analysis were normally distributed. The 'Versus Fits' plot did not indicate abnormalities in the variance, and there was not enough evidence to suspect non-constant variance. The 'Versus Order' plot did not exhibit unusual patterns. A validation experiment was then carried out to assess the validity of the regression analysis generated by Minitab.

$$width = 869.469 - 132.027F + 202.753P + 378.232V + 237.054S + 160.398PS \quad \ldots\ldots(3)$$

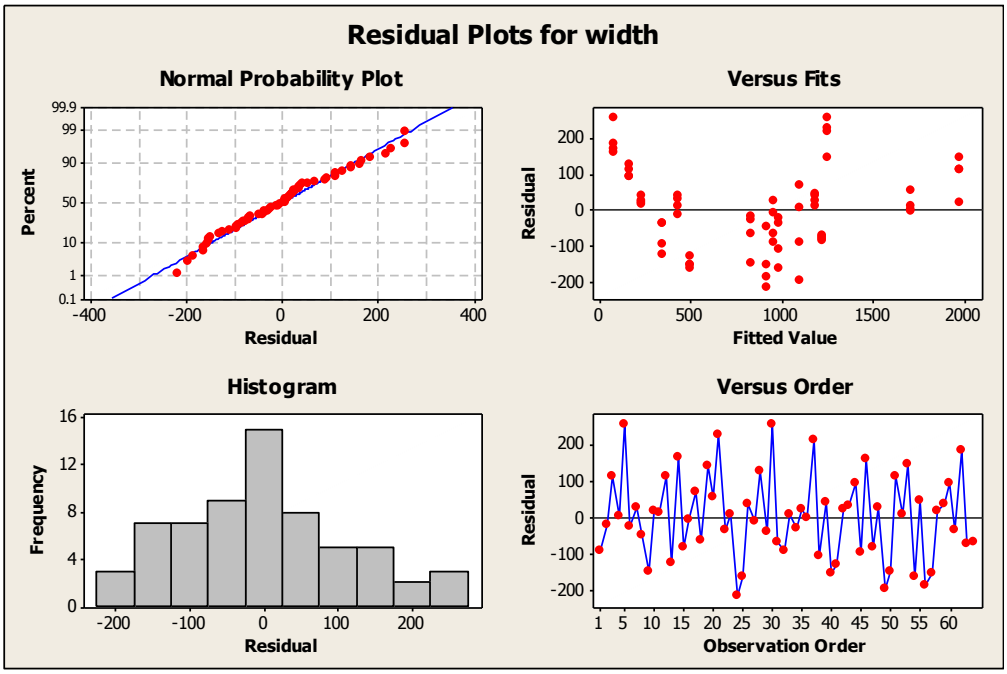

Figure 20: Residual plots of regression analysis of width from screening experiment

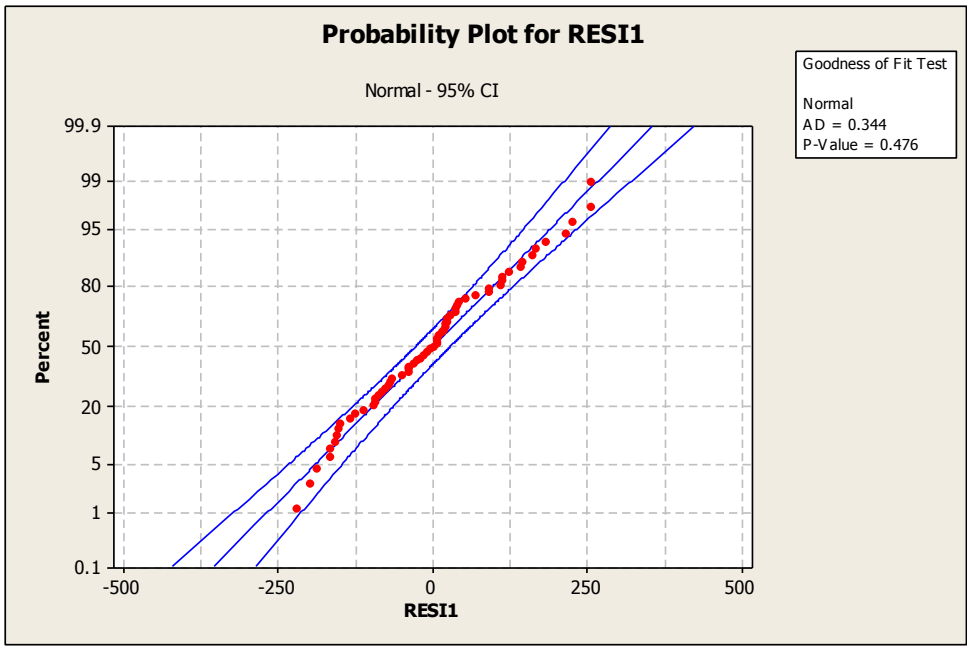

Figure 21: Normality test for residuals from regression analysis of width from screening experiment

3.2.3 Validation

A validation experiment was carried out at the center point levels of the significant factors in the regression model for height and width to check for curvature and model adequacy. Factor levels used in the experiment are discussed in Table 4. Due to apparatus limitations, namely least count of available syringes, solid loading fraction was set to a coded value of 0.04, viz. 3.16 g/ml or 6 grams of NiO-YSZ powder mixed with 1.9 ml of ink vehicle), instead of a coded value of 0 (which is 3.2 g/ml or 6 grams of NiO-YSZ powder was mixed with 1.67 ml of ink vehicle).

Table 4: Validation experiment process parameter settings

Parameter	Factor Levels (coded value)	
Feed (F)	7.5 mm/sec (0)	
Pressure (P)	15 PSI (0)	
Solid loading fraction (V)	3.16 g/ml (0.04)	
Standoff (S)	75 µm (0)	
Nozzle (N)	100 µm (-1)	125 µm (+1)
Valve position (VP)	1.7 mm (-1)	2.5 mm (+1)
Valve opening speed (VOS)	5 mm/sec (-1)	10 mm/sec (+1)
Wait (W)	0.1 sec (-1)	0.2 sec (+1)

Lines were printed with the settings mentioned above and were compared with the predicted values from the regression analysis. The comparison is tabulated in Table 5 and Table 6.

Table 5: Validation experiment output for height

Run #	Feed	Pressure	Solid loading fraction	Standoff	Nozzle	Valve position	Valve opening speed	Wait	Predicted value (µm)	Actual value (µm)
1	0	0	0.04	0	-1	-1	-1	-1	72.187	73.45
2	0	0	0.04	0	-1	-1	-1	-1	72.187	70.917
3	0	0	0.04	0	+1	+1	+1	+1	72.187	71.82
4	0	0	0.04	0	+1	+1	+1	+1	72.187	73.15

Table 6: Validation experiment output for width

Run #	Feed	Pressure	Solid loading fraction	Standoff	Nozzle	Valve position	Valve opening speed	Wait	Predicted value (µm)	Actual value (µm)
1	0	0	0.04	0	-1	-1	-1	-1	884.602	1094.24
2	0	0	0.04	0	-1	-1	-1	-1	884.602	1097.12
3	0	0	0.04	0	+1	+1	+1	+1	884.602	1193.9
4	0	0	0.04	0	+1	+1	+1	+1	884.602	1204.627

The validation experiment for height showed a less than 2% error between the predicted and actual values. It was observed that the error was within the prediction interval (standard error, ±13.7291) of the regression model. The standard error of the regression model can be seen in the Minitab output from Appendix B.2. As this observed error lies within the prediction space of the model, it was concluded that there was no evidence to support curvature, and the regression model for height was valid.

The validation experiment for width showed a very large difference between the predicted and actual values, over 24%. It was observed that the error was outside the prediction interval (standard error, ±119.784) of the regression model. The standard error of the regression model can be seen in the Minitab output from Appendix B.3. This large observed error was indicative of curvature, and a higher order design was required to fit a regression model to the output width of the process.

Comments

Considering the graph in Figure 14 from the preliminary experiment, it was observed that the nozzle diameter noticeably affected the width of a printed track. However, looking at the half normal plot from the width screening analysis in Figure 19 and the Minitab factorial analysis in Appendix B.3, it was observed that nozzle diameter was not statistically significant. It was hypothesized that the use of lower solid loading fraction pastes in the screening experiment as discussed previously was the cause of this phenomenon. Lowering the solid loading fraction of the pastes reduces their viscosity and contributes to post deposition paste flow-out. In the screening experiment, the facts that the viscosities of the pastes were relatively low (compared with the preliminary experiment) and the samples were allowed to air dry for 24 hours before measurement allowed flow-out to become a more dominant factor (as compared with nozzle diameter) in its effect on the height and width of a printed track. The amount of flow-out, and hence the width and height of the printed track, are also strongly influenced by the surface wetting properties of the paste and the surface energies of the paste and the substrate [36]. These properties have not been studied in the scope of this thesis and will require further investigation in future studies.

3.3 Higher Order Model

Since the two-level model discussed for width analysis in Section 3.2 was unable to adequately predict the width result of the validation experiment, a higher order model was deemed necessary. A three level design within the same high and low factor settings for the significant factors from the previous experiment were chosen. The third level for all of the factors was the center point (half-way between the high and low factor settings). A three level four factor randomized full factorial experiment was generated using Minitab. To overcome the issues with randomization of pressure discussed in Section 3.2 for the screening experiment, an entire system cleanup was performed after each run. Factor levels for the higher order model are tabulated in Table 7.

Table 7: Factor levels for higher order experiment

Factor	Low (-1)	Mid (0)	High (+1)
Feed (F)	5 mm/sec	7.5 mm/sec	10 mm/sec
Pressure (P)	10 PSI	15 PSI	20 PSI
Solid loading fraction (V)	2.4 g/ml	3.2 g/ml	4.8 g/ml
Standoff (S)	50 µm	75 µm	100 µm

All insignificant factors were set at their high levels from the screening experiment. The 125 µm inner diameter (ID) nozzle was used. Valve position was set to 2.5 mm, and a valve opening speed of 10mm/sec was used. Motion delay, or wait, was set to 0.2 sec. The 3^4 full factorial experiment was run, and the data collected was analyzed in Minitab using a general regression analysis. Four lines were printed for each setting, and their average width was used as the response width for each setting. Data from the experiment is presented in Appendix C.1,

Table 13.

A best subset regression analysis was performed using Minitab. A best subset regression analysis considers multiple subset models of specified factors and interactions, and it calculates R^2 values for each subset. The analysis then compares the precision and bias of all subset models using a statistic called Mallow's C_p. A lower Mallow's C_p value indicates a better fit. The model with the lowest Mallow's C_p was selected for regression analysis. The Minitab output for the best subset regression analysis is given in Appendix C.2. Based on Table 14, the regression model with the best fit (lowest Mallow's $C_{p)}$ was observed as the highlighted row and was used to generate a regression equation for width as a function of the feed (F), pressure (P), solid loading fraction (V) and standoff (S). This is given in equation (4).

$$W = 1253 - 166F + 194P + 833V + 154S - 44FP - 107FV - 48FS + 182PV - 168VV + 102VS$$

…… (4)

The residual plots from the regression analysis are shown in Figure 22. The normal probability plot and histogram displayed normality of residuals, but a verification test for normality was conducted in Minitab. Figure 23 shows a normal probability plot of the residuals with a goodness of fit test. The p-value was observed to be 0.289. Hence it was concluded that residuals for this analysis were normally distributed. The 'Versus Fits' plot did not indicate abnormalities in the variance, and there was not enough evidence to suspect non-constant variance. The 'Versus Order' plot did not exhibit any patterns. The next step was to validate the model generated during this regression analysis.

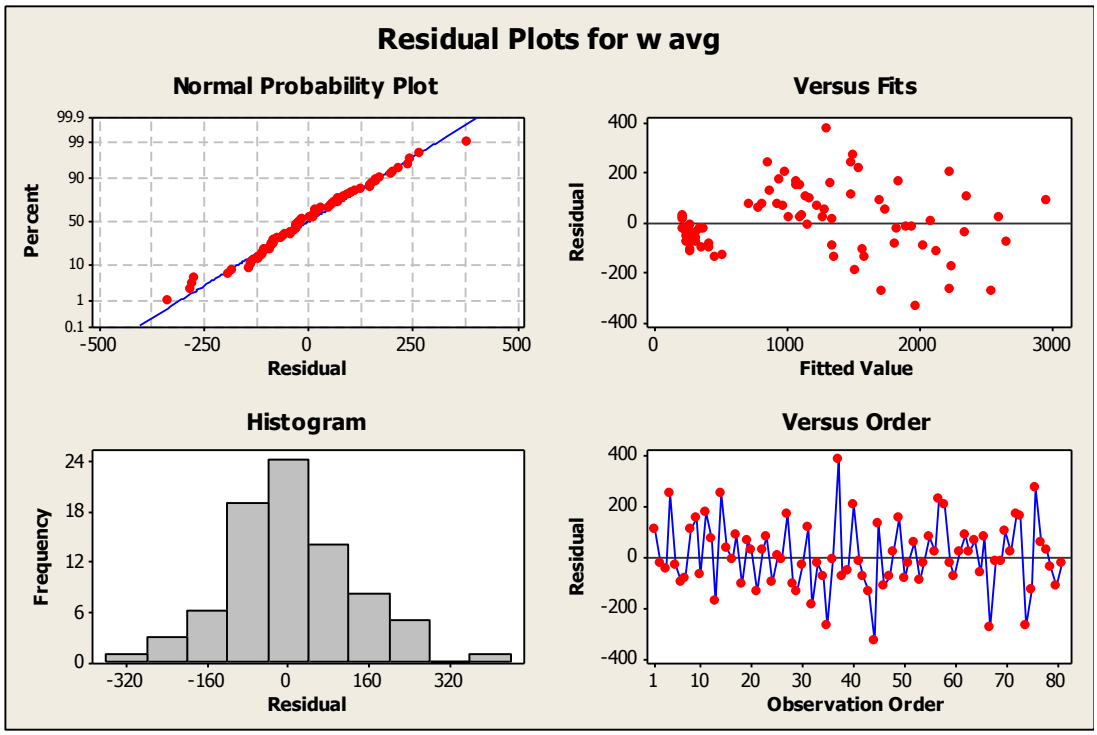

Figure 22: Residual plots of regression analysis of width from higher order model

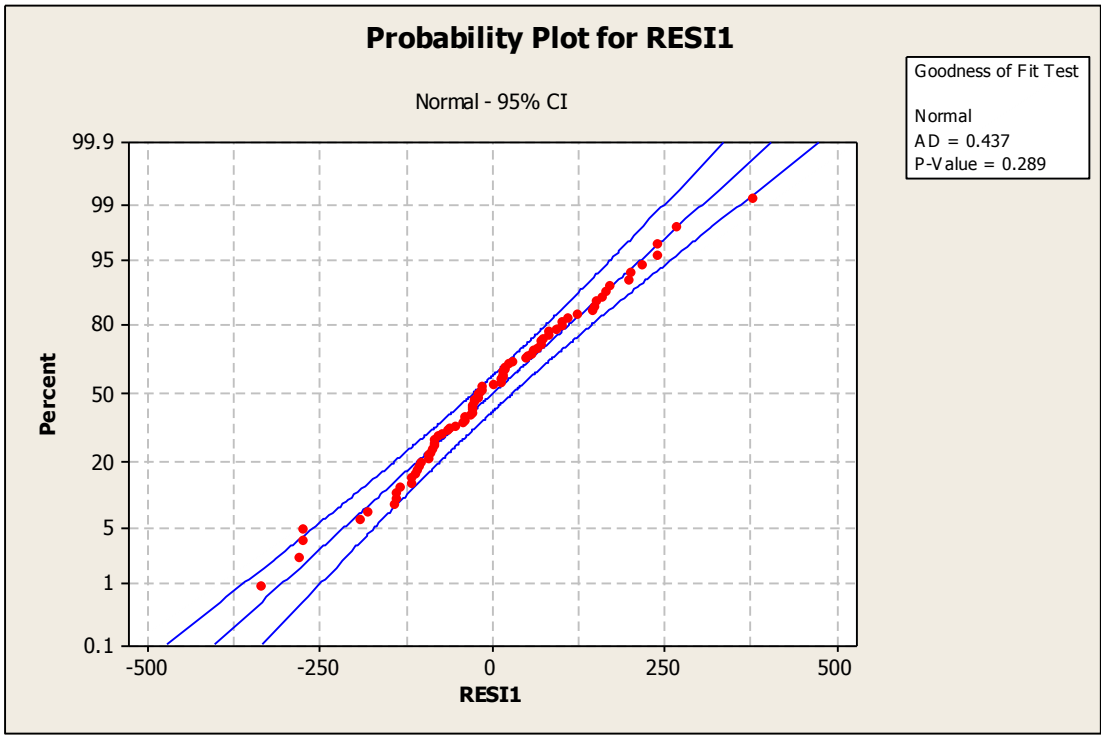

Figure 23: Normality test for residuals from regression analysis of width from higher order model

3.3.1 Validation for Higher Order Regression

In order to test the validity of the model within the design space, intermediate parameter settings were used that were not a part of the higher order experiment. The settings used for validation are tabulated in Table 8.

Table 8: Factor levels for validation of higher order experiment

Run #	Setting 1 (-0.5)	Setting 2 (+0.5)
Feed (F)	6.25 mm/sec	8.75 mm/sec
Pressure (P)	12.5 PSI	17.5 PSI
Solid loading fraction (V)	2.75 g/ml	3.84 g/ml
Standoff (S)	62.5 µm	87.5 µm

Other input parameters were set to the same values as in the higher order experiment, i.e.

1. Nozzle = 125µm
2. Valve position = 2.5mm
3. Valve opening speed = 10mm/sec
4. Wait = 0.2 sec

Lines were printed with the settings mentioned above and were compared to the predicted values from the regression analysis. The comparison is tabulated in Table 9.

Table 9: Data from validation experiment of higher order experiment

Run #	Feed	Pressure	Solid loading fraction	Standoff	Predicted Value (µm)	Actual Values (µm)
1	-0.5	-0.5	-0.5	-0.5	818.25	844.67
2	-0.5	-0.5	-0.5	-0.5	818.25	825.418
3	+0.5	+0.5	+0.5	+0.5	1469.25	1480.51
4	+0.5	+0.5	+0.5	+0.5	1469.25	1478.24

Comparing the two regression models for width, viz. the screening experiment model and the higher order experiment model, we see that the standard error of 110.762 µm from the higher order experiment (Appendix C.2) is lower than the standard error of 119.784 µm from the screening experiment (Appendix B.3). The R-squared values for the higher order model (R-Sq = 98.12%, R-Sq(adj) = 97.86%, R-Sq(pred) = 97.50%, from Appendix C.2) are also better than those for the screening experiment (R-Sq = 95.61% , R-Sq(adj) = 95.24%, R-Sq(pred) = 94.66%, from Appendix B.3). The validation runs for the higher order experiment show a reduced error with a maximum of 3% as compared with the screening experiment which clearly exhibited its inability to model the existing curvature in the model. Also looking at the main effects and interaction plots in Appendix C.2, Figure 24 and Figure 25, we see that the solid loading fraction is the main contributor to the curvature present in the model.

Chapter 4

Conclusions and Recommendations

4.1 Summary

As proposed in Section 2.2, the objective of this thesis was to develop a mathematical model to predict the dimensional properties, viz. the height and width of the deposited track, based on a given set of input parameters for the nScrypt tabletop material dispensing system with the SmartPump tool. A brief investigation of the process revealed a set of eight process parameters that are user controllable, viz. feed, extrusion or air pressure, nozzle inner diameter, paste viscosity (which was quantified as the solid loading fraction of the paste for the scope of this dissertation), standoff distance, valve position, valve opening and closing speed and motion delay or wait. An initial experiment varying only the pressure and nozzle diameter was conducted in order to check the feasibility of application of regression for prediction of the width of printed lines. Once deemed feasible, an eight-factor-two-level fractional factorial, 2^{8-4}, experiment was run for screening. The response variables in this experiment were height and width of the printed track and were analyzed independently using factorial analysis to identify significant parameters. Process parameters that significantly affected the height of a printed line were air pressure, solid loading fraction of the paste and standoff distance. The process parameters significantly affecting width were feed rate, air pressure, solid loading fraction and standoff distance. The significant parameters where then analyzed using regression analysis. Separate equations were obtained for height and width.

$$height = 71.6232 + 11.5462P + 14.105V + 7.4483S \quad \ldots\ldots(2)$$

$$width = 869.469 - 132.027F + 202.753P + 378.232V + 237.054S + 160.398PS \quad \ldots\ldots(3)$$

A validation experiment revealed that although the regression model for height response was acceptable (a maximum error of less than 2% was observed), that for width was not (an error of over 25% was

observed). Evidence suggesting curvature in the width regression model was observed. A higher order experiment was designed for the width response using only the significant factors obtained from the screening experiment. This time, a four-factor-three-level full factorial (3^4) experiment was designed to account for curvature in the model. The regression model generated from this analysis was found to have a lower standard error, and an improved set of R-square values was obtained.

$$W = 1253 - 166F + 194P + 833V + 154S - 44FP - 107FV - 48FS + 182PV - 168VV + 102VS$$

…… (4)

This model was found to be better at predicting center point values as well as intermediate values not considered in the experiment (maximum error was found to be less than 3%). The regression analysis was concluded at this stage with equations (2) and (4) as the accepted predictors for height and width respectively.

4.2 Contributions

The work described in this thesis contributing to the analysis of slurry based micro-extrusion direct-writing can be summarized as follows:

1. A comprehensive study of the effects of varying all user controlled process parameters simultaneously on the dimensional properties, namely height and width, of lines printed using the nScrypt SmartPump. This research studies the quantitative the effect of the solid loading fraction (and hence viscosity) of a paste on the dimensions of printed lines and identifies it as the parameter that has the largest effect. It revealed that in pastes with lower solid loading fractions lateral flow of paste after deposition becomes prominent and affects line width.
2. A simple two step approach employing design of experiments as the first step and regression analysis as the second step was utilized. This approach can also be adapted to other slurry extrusion based additive manufacturing processes which involve similar process parameters, namely stage translation speed (job feed rate), viscosity (or solid loading fraction), nozzle diameter (orifice size), pressure (or material feed rate), and standoff distance.

3. The regression equations developed in this research can be used to predict process output and hence be used to make decisions about the process parameters that must be used for a particular application.

4.3 Future Work Recommendations

The analysis in this thesis used the identical powder and ink vehicle for paste preparation. A wide variety of powders and solvents are available. Different powders and solvents when mixed in different proportions produce vastly different rheological properties of pastes. Although pastes having different solid loading fractions were considered in this work, the effects of different particle sizes and shapes need to be investigated. Particle size and shape (i.e. spherical versus irregular) can greatly affect the behavior of the paste in terms of viscosity and printability. A limited range of process parameter values was analyzed in this thesis, and further investigation into settings beyond the design space is required. The pastes used in this thesis had viscosities in the lower spectrum of machine capability, so higher viscosities should be investigated. As discussed in Section 3.2, surface tension and surface energy of pastes and how they interact with the surface energy of the substrate needs to be looked into. The change in the contact angle of low viscosity pastes on the substrate with respect to time as the paste flows out and dries after deposition also needs characterization. A lower range of nozzle diameters and a much larger range of pressures are also available for inspection.

The effects of sintering on the dimensional properties of printed lines have not been studied. Thermal deformation and surface bonding properties of materials due to elevated temperatures, and heating and cooling rates can be explored. All samples in this research were printed at room temperature on the same substrate. Further research into printing on different substrates and their effect on paste flow and line dimensions is required as well as the effects of printing on substrates at lowered and elevated temperatures is required. These factors affect the surface tension and energy and will hence affect line dimensions. At lower temperatures, similar to freeze tape casting, the solvent will freeze post deposition. At elevated temperatures effects of solvent viscosity change and solvent evaporation may also come into play. These effects may be beneficial or detrimental to the process and need investigation.

Two phases of a process similar to the work by Deng et al. [31] discussed in Section 2.3 have been completed, but the application of an optimization algorithm to the experimental data and regression analysis would give us a technique to select process parameters based on a target process output. Preliminary implementation of a simple non-linear model and AMPL (A Mathematical Programming

Language) using the MINOS solver showed its feasibility, but a more robust implementation is necessary to cover the entire design space.

Finally, investigation into different response parameters such as flow rate and cross sectional area of a printed track are required to completely characterize the nScrypt micro-extrusion process and validate the models proposed in this thesis. Results from these investigations along, with this thesis will allow us to use this methodology for similar extrusion based applications.

Bibliography

[1] P. F. Jacobs and D. T. Reid, *Rapid prototyping & manufacturing : fundamentals of stereolithography*. Dearborn, MI: Society of Manufacturing Engineers in cooperation with the Computer and Automated Systems Association of SME, 1992.

[2] I. Gibson, B. Stucker, and D. Rosen, *Additive Manufacturing Technologies: Rapid Prototyping to Direct Digital Manufacturing*: Springer Verlag, 2009.

[3] K. G. Cooper, *Rapid prototyping technology: selection and application*: CRC, 2001.

[4] J. P. Kruth, M. Leu, and T. Nakagawa, "Progress in additive manufacturing and rapid prototyping," *CIRP Annals-Manufacturing Technology*, vol. 47, pp. 525-540, 1998.

[5] P. Calvert, "Inkjet printing for materials and devices," *Chemistry of Materials*, vol. 13, pp. 3299-3305, 2001.

[6] D. T. Pham and R. S. Gault, "A comparison of rapid prototyping technologies," *International Journal of Machine Tools and Manufacture*, vol. 38, pp. 1257-1287, 1998.

[7] J. P. Kruth, X. Wang, T. Laoui, and L. Froyen, "Lasers and materials in selective laser sintering," *Assembly Automation*, vol. 23, pp. 357-371, 2003.

[8] W. Yeong, C. Chua, K. Leong, and M. Chandrasekaran, "Rapid prototyping in tissue engineering: challenges and potential," *TRENDS in Biotechnology*, vol. 22, pp. 643-652, 2004.

[9] K. K. B. Hon, L. Li, and I. M. Hutchings, "Direct writing technology--Advances and developments," *CIRP Annals - Manufacturing Technology*, vol. 57, pp. 601-620, 2008.

[10] A. Pique and D. B. Chrisey, *Direct-write technologies for rapid prototyping applications: sensors, electronics, and integrated power sources*: Academic Press, 2002.

[11] Y. Zhang, C. Liu, and D. Whalley, "Direct-write techniques for maskless production of microelectronics: a review of current state-of-the-art technologies," pp. 497-503, 2009.

[12] A. Piqué, S. A. Mathews, B. Pratap, R. C. Y. Auyeung, B. J. Karns, and S. Lakeou, "Embedding electronic circuits by laser direct-write," *Microelectronic engineering*, vol. 83, pp. 2527-2533, 2006.

[13] M. C. Wanke, O. Lehmann, K. Müller, Q. Wen, and M. Stuke, "Laser rapid prototyping of photonic band-gap microstructures," *Science*, vol. 275, pp. 1284-1286, 1997.

[14] T. Tong, J. Li, Q. Chen, J. P. Longtin, S. Tankiewicz, and S. Sampath, "Ultrafast laser micromachining of thermal sprayed coatings for microheaters: design, fabrication and characterization," *Sensors and Actuators A: Physical*, vol. 114, pp. 102-111, 2004.

[15] B. Li, P. A. Clark, and K. H. Church, "Robust Direct-Write Dispensing Tool and Solutions for Micro/Meso-Scale Manufacturing and Packaging," in *ASME 2007 International Manufacturing Science And Engineering Conference*, Atlanta, Georgia, USA, pp. 715-721, 2007.

[16] R. O. Kadara, N. Jenkinson, B. Li, K. H. Church, and C. E. Banks, "Manufacturing electrochemical platforms: Direct-write dispensing versus screen printing," *Electrochemistry Communications*, vol. 10, pp. 1517-1519, 2008.

[17] C. Xudong, K. Church, and Y. Haixin, "High speed non-contact printing for solar cell front side metallization," in *Photovoltaic Specialists Conference (PVSC), 2010 35th IEEE*, 2010, pp. 001343-001347.

[18] B. M. Blackburn, M. Camaratta, and E. D. Wachsman, "Advances in Rapid Prototyping for Solid State Ionics," *ECS Transactions*, vol. 16, pp. 367-379, 2009.

[19] A. J. Lopes, E. MacDonald, and R. B. Wicker, "Integrating stereolithography and direct print technologies for 3D structural electronics fabrication," *Rapid Prototyping Journal*, vol. 18, pp. 129-143, 2012.

[20] B. M. Blackburn, M. Camaratta, and E. D. Wachsman, "Advances in Rapid Prototyping for Solid State Ionics."

[21] J. Cesarano Iii, "Robocasting of ceramics and composites using fine particle suspensions," Sandia National Labs., Albuquerque, NM (US); Sandia National Labs., Livermore, CA (US)1999.

[22] J. Cesarano, R. Segalman, and P. Calvert, "ROBOCASTING PROVIDES MOULDLESS FABRICATION FROM SLURRY DEPOSITION," *Ceramic Industry*, vol. 148, pp. 94-96, 1998.

[23] J. E. Smay, T. B., and C. J. III, *Piezoelectric and Acoustic Materials for Transducer Applications: Chapter 15 - Robocasting of Three-Dimensional Piezoelectric Structures*: Springer, 2008.

[24] T. Huang, M. S. Mason, X. Zhao, G. E. Hilmas, and M. C. Leu, "Aqueous-based freeze-form extrusion fabrication of alumina components," *Rapid Prototyping Journal*, vol. 15, Iss: 2, pp. 88-95, 2009.

[25] H. B. Denham, J. Cesarano Iii, B. H. King, and P. Calvert, "Mechanical behavior of robocast alumina," in *Solid Freeform Fabrication Symposium*, pp. 589-596, 1998.

[26] J. Russias, *et al.*, "Fabrication and in vitro characterization of three-dimensional organic/inorganic scaffolds by robocasting," *Journal of Biomedical Materials Research Part A*, vol. 83, pp. 434-445, 2007.

[27] D. Rohner, D. W. Hutmacher, T. K. Cheng, M. Oberholzer, and B. Hammer, "In vivo efficacy of bone-marrow-coated polycaprolactone scaffolds for the reconstruction of orbital defects in the

pig," *Journal of Biomedical Materials Research Part B: Applied Biomaterials*, vol. 66, pp. 574-580, 2003.

[28] H. Otsuka, Y. Nagasaki, K. Kataoka, T. Okano, and Y. Sakurai, "Reactive PEG-polylactide block copolymer for tissue engineering," *Polymer Preprints(USA)*, vol. 39, Iss: 2, pp. 128-129, 1998.

[29] P. K. Bharti, M. I. Khan, and H. Singh, "RECENT METHODS FOR OPTIMIZATION OF PLASTIC INJECTION MOLDING PROCESS–A RETROSPECTIVE AND LITERATURE REVIEW," *International Journal of Engineering Science*, vol. 2, 2010.

[30] H. Oktem, T. Erzurumlu, and I. Uzman, "Application of Taguchi optimization technique in determining plastic injection molding process parameters for a thin-shell part," *Materials & Design*, vol. 28, pp. 1271-1278, 2007.

[31] W.-J. Deng, C.-T. Chen, C.-H. Sun, W.-C. Chen, and C.-P. Chen, "An effective approach for process parameter optimization in injection molding of plastic housing components," *Polymer - Plastics Technology and Engineering*, vol. 47, pp. 910-919, 2008.

[32] W.-C. Chen, G.-L. Fu, P.-H. Tai, and W.-J. Deng, "Process parameter optimization for MIMO plastic injection molding via soft computing," *Expert Systems with Applications*, vol. 36, pp. 1114-1122, 2009.

[33] J. G. Zhou, D. Herscovici, and C. C. Chen, "Parametric process optimization to improve the accuracy of rapid prototyped stereolithography parts," *International Journal of Machine Tools and Manufacture*, vol. 40, pp. 363-379, 2000.

[34] D. C. Montgomery, *Design and analysis of experiments*: John Wiley & Sons Inc, 2008.

[35] T. B. Barker, *Quality by experimental design* vol. 43: CRC Press, 1994.

[36] P. C. T. Centre. (14th Sept 2012, *Surface Tension, Surface Energy, Contact Angle and Adhesion*. Available: http://www.pra-world.com/technical_services/laboratory/testing/surface-tension

Appendix A: nScrypt Machine Code

```
absolute                        //uses absolute measurement system for this file
pen  SMARTPUMP_1                //selects the nScrypt SmartPump as the printing tool
speed    10                     //sets a value for the feed rate to 10 mm/s

trigvalverel      1.7     10    //sets valve opening to 1.7 mm and valve opening speed to 10 mm/s
trigwait 0.1                    //sets the motion delay, or wait, to 0.1 sec
move     0        20      0     //moves to coordinates X=0, Y=20 mm, and Z=0
valverel          0       10    //closes the valve, i.e. brings valve rod to 0 position at a speed of 10 mm/s
move     5        0       0     //moves to coordinates X=5 mm, Y=0, and Z=0
```

Appendix B: Screening Experiment

B.1 Screening Experiment Data

Table 10: Design table and data from the screening experiment

StdOrder	RunOrder	F	P	N	V	S	VP	VOS	W	height	width
1	1	-1	-1	-1	1	-1	-1	-1	-1	80.63	1007.22
17	2	-1	-1	-1	1	-1	-1	-1	-1	65.34	1170.20
33	3	-1	-1	-1	1	-1	-1	-1	-1	68.24	1107.80
49	4	-1	-1	-1	1	-1	-1	-1	-1	76.95	904.07
2	5	1	-1	-1	1	-1	1	1	1	63.52	816.21
18	6	1	-1	-1	1	-1	1	1	1	53.20	770.37
34	7	1	-1	-1	1	-1	1	1	1	51.92	807.30
50	8	1	-1	-1	1	-1	1	1	1	43.79	687.61
3	9	-1	1	-1	1	1	-1	1	1	96.67	2094.00
19	10	-1	1	-1	1	1	-1	1	1	95.87	2124.00
35	11	-1	1	-1	1	1	-1	1	1	98.71	2001.00
51	12	-1	1	-1	1	1	-1	1	1	105.57	2094.00
4	13	1	1	-1	1	1	1	-1	-1	101.47	1718.00
20	14	1	1	-1	1	1	1	-1	-1	121.26	1770.00
36	15	1	1	-1	1	1	1	-1	-1	93.12	1712.00
52	16	1	1	-1	1	1	1	-1	-1	121.78	1724.00
5	17	-1	-1	1	1	1	1	1	-1	95.17	1510.00
21	18	-1	-1	1	1	1	1	1	-1	106.62	1481.00
37	19	-1	-1	1	1	1	1	1	-1	81.33	1470.00
53	20	-1	-1	1	1	1	1	1	-1	97.45	1400.00
6	21	1	-1	1	1	1	-1	-1	1	63.99	965.19
22	22	1	-1	1	1	1	-1	-1	1	59.19	952.46
38	23	1	-1	1	1	1	-1	-1	1	51.90	879.88
54	24	1	-1	1	1	1	-1	-1	1	51.28	825.13
7	25	-1	1	1	1	-1	1	-1	1	95.42	1210.00

23	26	-1	1	1	1	-1	1	-1	1	118.83	1194.00
39	27	-1	1	1	1	-1	1	-1	1	92.97	1225.00
55	28	-1	1	1	1	-1	1	-1	1	83.95	1229.00
8	29	1	1	1	1	-1	-1	1	-1	90.35	872.00
24	30	1	1	1	1	-1	-1	1	-1	111.28	703.00
40	31	1	1	1	1	-1	-1	1	-1	106.52	768.00
56	32	1	1	1	1	-1	-1	1	-1	99.04	734.00
9	33	-1	-1	-1	-1	1	1	-1	1	56.63	344.58
25	34	-1	-1	-1	-1	1	1	-1	1	61.56	332.18
41	35	-1	-1	-1	-1	1	1	-1	1	59.81	365.76
57	36	-1	-1	-1	-1	1	1	-1	1	59.56	340.96
10	37	1	-1	-1	-1	1	-1	1	-1	45.71	249.41
26	38	1	-1	-1	-1	1	-1	1	-1	54.36	271.11
42	39	1	-1	-1	-1	1	-1	1	-1	48.72	255.33
58	40	1	-1	-1	-1	1	-1	1	-1	50.77	250.99
11	41	-1	1	-1	-1	-1	1	1	-1	45.04	439.12
27	42	-1	1	-1	-1	-1	1	1	-1	66.16	415.87
43	43	-1	1	-1	-1	-1	1	1	-1	54.94	459.26
59	44	-1	1	-1	-1	-1	1	1	-1	40.96	466.57
12	45	1	1	-1	-1	-1	-1	-1	1	45.51	275.84
28	46	1	1	-1	-1	-1	-1	-1	1	41.23	290.06
44	47	1	1	-1	-1	-1	-1	-1	1	39.58	257.70
60	48	1	1	-1	-1	-1	-1	-1	1	43.37	256.91
13	49	-1	-1	1	-1	-1	-1	1	1	47.08	219.42
29	50	-1	-1	1	-1	-1	-1	1	1	40.88	305.05
45	51	-1	-1	1	-1	-1	-1	1	1	46.48	248.22
61	52	-1	-1	1	-1	-1	-1	1	1	57.21	306.63
14	53	1	-1	1	-1	-1	1	-1	-1	43.29	247.98
30	54	1	-1	1	-1	-1	1	-1	-1	53.65	337.34
46	55	1	-1	1	-1	-1	1	-1	-1	42.23	241.91
62	56	1	-1	1	-1	-1	1	-1	-1	44.05	263.62
15	57	-1	1	1	-1	1	-1	-1	-1	88.56	1142.47
31	58	-1	1	1	-1	1	-1	-1	-1	85.04	1153.55
47	59	-1	1	1	-1	1	-1	-1	-1	89.18	1138.19

63	60	-1	1	1	-1	1	-1	-1	-1	84.03	1148.75
16	61	1	1	1	-1	1	1	1	1	72.20	951.06
32	62	1	1	1	-1	1	1	1	1	79.09	868.52
48	63	1	1	1	-1	1	1	1	1	74.82	984.65
64	64	1	1	1	-1	1	1	1	1	78.91	890.60

Table 11: Mean and standard deviation for screening experiment width data

Run Order	Width 1	Width 2	Width 3	Width 4	Average width	Standard deviation
1-4	1007.22	1170.20	1107.80	904.07	1047.32	101.1019
5-8	816.21	770.37	807.30	687.61	770.37	50.78232
9-12	2094.00	2124.00	2001.00	2094.00	2078.25	46.25135
13-16	1718.00	1770.00	1712.00	1724.00	1731.00	22.91288
17-20	1510.00	1481.00	1470.00	1400.00	1465.25	40.40653
21-24	965.19	952.46	879.88	825.13	905.67	56.75562
25-28	1210.00	1194.00	1225.00	1229.00	1214.50	13.79311
29-32	872.00	703.00	768.00	734.00	769.25	63.62144
33-36	344.58	332.18	365.76	340.96	345.87	12.33609
37-40	249.41	271.11	255.33	250.99	256.71	8.594013
41-44	439.12	415.87	459.26	466.57	445.20	19.69634
45-48	275.84	290.06	257.70	256.91	270.13	13.77655
49-52	219.42	305.05	248.22	306.63	269.83	37.42709
53-56	247.98	337.34	241.91	263.62	272.71	38.14521
57-60	1142.47	1153.55	1138.19	1148.75	1145.74	5.868895
61-64	951.06	868.52	984.65	890.60	923.71	46.37671
					Average standard deviation	**36.11538**

Table 12: Mean and standard deviation for screening experiment height data

Run Order	Height 1	Height 2	Height 3	Height 4	Average height	Standard deviation
1-4	80.63	65.34	68.24	76.95	72.79	6.227714
5-8	63.52	53.20	51.92	43.79	53.11	7.012531
9-12	96.67	95.87	98.71	105.57	99.20	3.819301
13-16	101.47	121.26	93.12	121.78	109.41	12.46897
17-20	95.17	106.62	81.33	97.45	95.14	9.051953
21-24	63.99	59.19	51.90	51.28	56.59	5.282816
25-28	95.42	118.83	92.97	83.95	97.79	12.87572
29-32	90.35	111.28	106.52	99.04	101.80	7.919058
33-36	56.63	61.56	59.81	59.56	59.39	1.768753
37-40	45.71	54.36	48.72	50.77	49.89	3.145402
41-44	45.04	66.16	54.94	40.96	51.78	9.735766
45-48	45.51	41.23	39.58	43.37	42.42	2.233419
49-52	47.08	40.88	46.48	57.21	47.91	5.886742
53-56	43.29	53.65	42.23	44.05	45.80	4.574886
57-60	88.56	85.04	89.18	84.03	86.70	2.20833
61-64	72.20	79.09	74.82	78.91	76.25	2.901095
					Average standard deviation	**6.069528**

B.2 Screening Experiment for Height – Minitab Output

Factorial Fit: height versus F, P, N, V, S, VP, VOS, W

Estimated Effects and Coefficients for height (coded units)

Term	Effect	Coef	SE Coef	T	P
Constant		71.62	1.007	71.16	0.000
F	-9.43	-4.72	1.007	-4.68	0.000
P	23.09	11.55	1.007	11.47	0.000
N	8.75	4.37	1.007	4.35	0.000
V	-28.21	-14.11	1.007	-14.01	0.000
S	14.90	7.45	1.007	7.40	0.000
VP	3.92	1.96	1.007	1.95	0.057
VOS	0.52	0.26	1.007	0.26	0.796
W	-10.08	-5.04	1.007	-5.01	0.000
F*P	8.03	4.02	1.007	3.99	0.000
F*N	-2.35	-1.17	1.007	-1.17	0.250
F*V	1.58	0.79	1.007	0.78	0.437
F*S	-2.64	-1.32	1.007	-1.31	0.195
F*VP	4.55	2.27	1.007	2.26	0.028
F*VOS	6.18	3.09	1.007	3.07	0.004
F*W	-9.55	-4.78	1.007	-4.74	0.000

S = 8.05210 PRESS = 5532.70

R-Sq = 91.39% R-Sq(pred) = 84.68% R-Sq(adj) = 88.69%

Analysis of Variance for height (coded units)

Source	DF	Seq SS	Adj SS	Adj MS	F	P
Main Effects	8	29338.8	29338.8	3667.4	56.56	0.000
F	1	1422.8	1422.8	1422.8	21.94	0.000
P	1	8532.2	8532.2	8532.2	131.60	0.000
N	1	1225.0	1225.0	1225.0	18.89	0.000
V	1	12732.9	12732.9	12732.9	196.39	0.000
S	1	3550.5	3550.5	3550.5	54.76	0.000
VP	1	246.0	246.0	246.0	3.79	0.057
VOS	1	4.4	4.4	4.4	0.07	0.796
W	1	1625.1	1625.1	1625.1	25.06	0.000
2-Way Interactions	7	3673.9	3673.9	524.8	8.09	0.000
F*P	1	1031.9	1031.9	1031.9	15.92	0.000

F*N	1	88.1	88.1	88.1	1.36	0.250
F*V	1	39.8	39.8	39.8	0.61	0.437
F*S	1	111.9	111.9	111.9	1.73	0.195
F*VP	1	330.8	330.8	330.8	5.10	0.028
F*VOS	1	611.7	611.7	611.7	9.43	0.004
F*W	1	1459.8	1459.8	1459.8	22.51	0.000
Residual Error	48	3112.1	3112.1	64.8		
Pure Error	48	3112.1	3112.1	64.8		
Total	63	36124.9				

Unusual Observations for height

Obs	StdOrder	height	Fit	SE Fit	Residual	St Resid
23	23	118.833	97.794	4.026	21.039	3.02R
27	27	66.158	51.777	4.026	14.381	2.06R
36	36	93.120	109.406	4.026	-16.286	-2.34R

R denotes an observation with a large standardized residual.

Alias Structure (up to order 3)

I

F + P*N*VOS + P*V*W + P*S*VP + N*V*VP + N*S*W + V*S*VOS + VP*VOS*W

P + F*N*VOS + F*V*W + F*S*VP + N*V*S + N*VP*W + V*VP*VOS + S*VOS*W

N + F*P*VOS + F*V*VP + F*S*W + P*V*S + P*VP*W + V*VOS*W + S*VP*VOS

V + F*P*W + F*N*VP + F*S*VOS + P*N*S + P*VP*VOS + N*VOS*W + S*VP*W

S + F*P*VP + F*N*W + F*V*VOS + P*N*V + P*VOS*W + N*VP*VOS + V*VP*W

VP + F*P*S + F*N*V + F*VOS*W + P*N*W + P*V*VOS + N*S*VOS + V*S*W

VOS + F*P*N + F*V*S + F*VP*W + P*V*VP + P*S*W + N*V*W + N*S*VP

W + F*P*V + F*N*S + F*VP*VOS + P*N*VP + P*S*VOS + N*V*VOS + V*S*VP

F*P + N*VOS + V*W + S*VP

F*N + P*VOS + V*VP + S*W

F*V + P*W + N*VP + S*VOS

F*S + P*VP + N*W + V*VOS

F*VP + P*S + N*V + VOS*W

F*VOS + P*N + V*S + VP*W

F*W + P*V + N*S + VP*VOS

General Regression Analysis: height versus P, V, S

Regression Equation

height = 71.6232 + 11.5462 P + 14.105 V + 7.4483 S

Coefficients

Term	Coef	SE Coef	T	P
Constant	71.6232	1.71614	41.7352	0.000
P	11.5462	1.71614	6.7280	0.000
V	-14.1050	1.71614	-8.2191	0.000
S	7.4483	1.71614	4.3402	0.000

Summary of Model

S = 13.7291 R-Sq = 68.69% R-Sq(adj) = 67.13%

PRESS = 11633.1 R-Sq(pred) = 64.38%

Analysis of Variance

Source	DF	Seq SS	Adj SS	Adj MS	F	P
Regression	3	24815.6	24815.6	8271.9	43.8855	0.0000000
P	1	8532.2	8532.2	8532.2	45.2666	0.0000000
V	1	12732.9	12732.9	12732.9	67.5529	0.0000000
S	1	3550.5	3550.5	3550.5	18.8370	0.0000555
Error	60	11309.3	11309.3	188.5		
Lack-of-Fit	4	3627.2	3627.2	906.8	6.6103	0.0001979
Pure Error	56	7682.1	7682.1	137.2		
Total	63	36124.9				

Fits and Diagnostics for Unusual Observations

Obs	height	Fit	SE Fit	Residual	St Resid
23	118.833	89.8262	3.43227	29.0068	2.18209R
38	51.904	81.6303	3.43227	-29.7263	-2.23621R
54	51.277	81.6303	3.43227	-30.3533	-2.28338R

R denotes an observation with a large standardized residual.

B.3 Screening Experiment for Width – Minitab Output

Factorial Fit: width versus F, P, N, V, S, VP, VOS, W

Estimated Effects and Coefficients for width (coded units)

Term	Effect	Coef	SE Coef	T	P
Constant		869.5	6.292	138.19	0.000
F	-264.1	-132.0	6.292	-20.98	0.000
P	405.5	202.8	6.292	32.23	0.000
N	2.7	1.4	6.292	0.22	0.829
V	-756.5	-378.2	6.292	-60.12	0.000
S	474.1	237.1	6.292	37.68	0.000
VP	53.2	26.6	6.292	4.23	0.000
VOS	5.7	2.9	6.292	0.45	0.652
W	-44.4	-22.2	6.292	-3.53	0.001
F*P	-33.4	-16.7	6.292	-2.65	0.011
F*N	-41.9	-21.0	6.292	-3.33	0.002
F*V	143.2	71.6	6.292	11.38	0.000
F*S	-40.5	-20.2	6.292	-3.21	0.002
F*W	4.4	2.2	6.292	0.35	0.728
P*S	320.8	160.4	6.292	25.49	0.000
V*S	-120.6	-60.3	6.292	-9.58	0.000

S = 50.3333 PRESS = 216187

R-Sq = 99.36% R-Sq(pred) = 98.86% R-Sq(adj) = 99.16%

Analysis of Variance for width (coded units)

Source	DF	Seq SS	Adj SS	Adj MS	F	P
Main Effects	8	16576262	16576262	2072033	817.87	0.000
F	1	1115587	1115587	1115587	440.34	0.000
P	1	2630955	2630955	2630955	1038.49	0.000
N	1	119	119	119	0.05	0.829
V	1	9155821	9155821	9155821	3613.98	0.000
S	1	3596467	3596467	3596467	1419.60	0.000
VP	1	45309	45309	45309	17.88	0.000
VOS	1	521	521	521	0.21	0.652
W	1	31483	31483	31483	12.43	0.001
2-Way Interactions	7	2279717	2279717	325674	128.55	0.000
F*P	1	17796	17796	17796	7.02	0.011

F*N	1	28148	28148	28148	11.11	0.002
F*V	1	328125	328125	328125	129.52	0.000
F*S	1	26184	26184	26184	10.34	0.002
F*W	1	311	311	311	0.12	0.728
P*S	1	1646555	1646555	1646555	649.93	0.000
V*S	1	232597	232597	232597	91.81	0.000
Residual Error	48	121605	121605	2533		
Pure Error	48	121605	121605	2533		
Total	63	18977584				

Unusual Observations for width

Obs	StdOrder	width	Fit	SE Fit	Residual	St Resid
8	8	872.00	769.25	25.17	102.75	2.36R
17	17	1170.20	1047.32	25.17	122.88	2.82R
49	49	904.07	1047.32	25.17	-143.25	-3.29R

R denotes an observation with a large standardized residual.

Alias Structure (up to order 3)

I

F + P*N*VOS + P*V*W + P*S*VP + N*V*VP + N*S*W + V*S*VOS + VP*VOS*W

P + F*N*VOS + F*V*W + F*S*VP + N*V*S + N*VP*W + V*VP*VOS + S*VOS*W

N + F*P*VOS + F*V*VP + F*S*W + P*V*S + P*VP*W + V*VOS*W + S*VP*VOS

V + F*P*W + F*N*VP + F*S*VOS + P*N*S + P*VP*VOS + N*VOS*W + S*VP*W

S + F*P*VP + F*N*W + F*V*VOS + P*N*V + P*VOS*W + N*VP*VOS + V*VP*W

VP + F*P*S + F*N*V + F*VOS*W + P*N*W + P*V*VOS + N*S*VOS + V*S*W

VOS + F*P*N + F*V*S + F*VP*W + P*V*VP + P*S*W + N*V*W + N*S*VP

W + F*P*V + F*N*S + F*VP*VOS + P*N*VP + P*S*VOS + N*V*VOS + V*S*VP

F*P + N*VOS + V*W + S*VP

F*N + P*VOS + V*VP + S*W

F*V + P*W + N*VP + S*VOS

F*S + P*VP + N*W + V*VOS

F*W + P*V + N*S + VP*VOS

F*VP + P*S + N*V + VOS*W

F*VOS + P*N + V*S + VP*W

General Regression Analysis: width versus F, P, V, S

Regression Equation

width = 869.469 - 132.027 F + 202.753 P + 378.232 V + 237.054 S + 160.398 P*S

Coefficients

Term	Coef	SE Coef	T	P
Constant	869.469	14.9730	58.0691	0.000
F	-132.027	14.9730	-8.8176	0.000
P	202.753	14.9730	13.5412	0.000
V	-378.232	14.9730	-25.2609	0.000
S	237.054	14.9730	15.8321	0.000
P*S	160.398	14.9730	10.7124	0.000

Summary of Model

S = 119.784	R-Sq = 95.61%	R-Sq(adj) = 95.24%
PRESS = 1013283	R-Sq(pred) = 94.66%	

Analysis of Variance

Source	DF	Seq SS	Adj SS	Adj MS	F	P
Regression	5	18145386	18145386	3629077	252.928	0.0000000
F	1	1115587	1115587	1115587	77.751	0.0000000
P	1	2630955	2630955	2630955	183.364	0.0000000
V	1	9155821	9155821	9155821	638.114	0.0000000
S	1	3596467	3596467	3596467	250.656	0.0000000
P*S	1	1646555	1646555	1646555	114.757	0.0000000
Error	58	832198	832198	14348		
Lack-of-Fit	10	710593	710593	71059	28.049	0.0000000
Pure Error	48	121605	121605	2533		
Total	63	18977584				

Fits and Diagnostics for Unusual Observations

Obs	width	Fit	SE Fit	Residual	St Resid
5	1510.00	1253.63	36.6763	256.368	2.24823R
30	337.34	79.80	36.6763	257.541	2.25852R

R denotes an observation with a large standardized residual.

Appendix C: Higher Order Experiment for Width

C.1 Experimental Data

Table 13: Design table and data from higher order experiment for width

StdOrder	RunOrder	Feed	Pressure	Solid loading fraction	Standoff	Average Width
41	1	0	0	0	0	1244.34
54	2	0	1	-1	1	345.19
71	3	1	0	-1	0	194.82
64	4	1	0	1	-1	1733.20
34	5	0	-1	-1	-1	203.12
26	6	-1	1	-1	0	316.69
9	7	-1	-1	-1	1	322.78
19	8	-1	1	1	-1	2465.63
33	9	0	-1	0	1	1249.84
44	10	0	0	-1	0	236.60
32	11	0	-1	0	0	1118.74
78	12	1	1	0	1	1296.39
11	13	-1	0	1	0	2066.20
4	14	-1	-1	0	-1	1109.79
81	15	1	1	-1	1	252.17
55	16	1	-1	1	-1	1145.20
21	17	-1	1	1	1	3053.73
62	18	1	-1	-1	0	169.30
68	19	1	0	0	0	1035.28
48	20	0	1	1	1	2623.33
29	21	0	-1	1	0	1459.40
77	22	1	1	0	0	1150.75
59	23	1	-1	0	0	896.90

17	24	-1	0	-1	0	264.50
46	25	0	1	1	-1	2096.67
52	26	0	1	-1	-1	253.52
30	27	0	-1	1	1	2017.67
57	28	1	-1	1	1	1466.00
18	29	-1	0	-1	1	325.41
53	30	0	1	-1	0	280.84
51	31	0	1	0	1	1600.00
1	32	-1	-1	1	-1	1332.00
36	33	0	-1	-1	1	317.44
35	34	0	-1	-1	0	216.32
12	35	-1	0	1	1	2275.75
10	36	-1	0	1	-1	1927.00
14	37	-1	0	0	0	1685.41
70	38	1	0	-1	-1	161.46
63	39	1	-1	-1	1	222.81
40	40	0	0	0	-1	1189.12
72	41	1	0	-1	1	232.33
73	42	1	1	1	-1	1739.83
56	43	1	-1	1	0	1229.00
38	44	0	0	1	0	1637.25
67	45	1	0	0	-1	993.84
61	46	1	-1	-1	-1	158.58
25	47	-1	1	-1	-1	241.12
76	48	1	1	0	-1	1036.54
69	49	1	0	0	1	1228.14
74	50	1	1	1	0	1939.80
16	51	-1	0	-1	-1	240.65
42	52	0	0	0	1	1347.02
22	53	-1	1	0	-1	1250.55
45	54	0	0	-1	1	332.69
58	55	1	-1	0	-1	789.95
13	56	-1	0	0	-1	1122.80
23	57	-1	1	0	0	1763.85

39	58	0	0	1	1	2428.57
43	59	0	0	-1	-1	227.22
20	60	-1	1	1	0	2584.43
7	61	-1	-1	-1	-1	226.32
65	62	1	0	1	0	1783.35
28	63	0	-1	1	-1	1354.33
31	64	0	-1	0	-1	851.37
8	65	-1	-1	-1	0	246.09
60	66	1	-1	0	1	1000.64
37	67	0	0	1	-1	1439.00
66	68	1	0	1	1	1887.11
79	69	1	1	-1	-1	189.03
49	70	0	1	0	-1	1276.03
80	71	1	1	-1	0	232.09
5	72	-1	-1	0	0	1230.22
50	73	0	1	0	0	1488.21
75	74	1	1	1	1	1966.40
27	75	-1	1	-1	1	389.34
15	76	-1	0	0	1	1777.71
24	77	-1	1	0	1	1796.11
6	78	-1	-1	0	1	1289.09
47	79	0	1	1	0	2307.25
3	80	-1	-1	1	1	2014.00
2	81	-1	-1	1	0	1800.00

C.2 Regression Analysis

Table 14: Minitab output for best subset regression analysis

Best Subsets Regression: w avg versus F, P, ...

Response is w avg

Vars	R-Sq	R-Sq(adj)	Mallows Cp	S	F	P	V	S	FF	FP	FV	FS	PP	PV	PS	VV	VS	SS
1	81.8	81.6	570.5	324.27			X											
1	4.5	3.3	3330.9	743.94		X												
2	86.3	86	413.4	283.43		X	X											
2	85.1	84.7	455.9	295.52	X		X											
3	89.6	89.2	298.8	248.91	X	X	X											
3	89.1	88.7	315.9	254.55		X	X	X										
4	92.4	92	201.3	214.41	X	X	X	X										
4	92.2	91.8	208.2	217.09	X	X	X	X						X				
5	95	94.6	110.6	175.3	X	X	X	X						X				
5	93.5	93	163.8	199.54	X	X	X	X								X		
6	96.1	95.8	73.1	155.85	X	X	X	X						X		X		
6	95.9	95.5	80.2	159.78	X	X	X	X			X			X				
7	97	96.7	42.7	137.58	X	X	X	X			X			X		X		
7	96.9	96.6	46.1	139.72	X	X	X	X						X		X	X	
8	97.8	97.5	15.7	118.41	X	X	X	X			X			X		X	X	
8	97.2	96.8	38.3	134.33	X	X	X	X			X	X		X		X		
9	98	97.7	11.2	114.26	X	X	X	X			X	X		X		X	X	
9	97.9	97.7	12.4	115.14	X	X	X	X		X	X			X		X	X	
10	98.1	97.9	7.9	110.76	X	X	X	X		X	X	X		X		X	X	
10	98	97.7	12.7	114.66	X	X	X	X	X		X	X		X		X	X	
11	98.1	97.8	9.4	111.13	X	X	X	X	X	X	X	X		X		X	X	
11	98.1	97.8	9.7	111.39	X	X	X	X		X	X	X	X	X		X	X	
12	98.1	97.8	11.2	111.77	X	X	X	X	X	X	X	X	X	X		X	X	
12	98.1	97.8	11.2	111.77	X	X	X	X	X	X	X	X		X		X	X	X
13	98.1	97.8	13	112.42	X	X	X	X	X	X	X	X	X	X		X	X	X
13	98.1	97.8	13.2	112.6	X	X	X	X	X	X	X	X	X	X	X	X	X	
14	98.1	97.8	15	113.27	X	X	X	X	X	X	X	X	X	X	X	X	X	X

General Regression Analysis: w avg versus F, P, V, S, FP, FV, FS, PV, VV, VS

Regression Equation

w avg = 1252.54 - 166.412 F + 194.418 P + 832.845 V + 153.774 S - 43.5149 FP
- 107.459 FV - 47.8801 FS + 181.729 PV - 167.902 VV + 101.682 VS

Coefficients

Term	Coef	SE Coef	T	P
Constant	1252.54	21.3161	58.7603	0.000
F	-166.41	15.0728	-11.0406	0.000
P	194.42	15.0728	12.8986	0.000
V	-832.85	15.0728	-55.2550	0.000
S	153.77	15.0728	10.2021	0.000
FP	-43.51	18.4603	-2.3572	0.021
FV	107.46	18.4603	5.8211	0.000
FS	-47.88	18.4603	-2.5937	0.012
PV	-181.73	18.4603	-9.8443	0.000
VV	-167.90	26.1068	-6.4313	0.000
VS	-101.68	18.4603	-5.5082	0.000

Summary of Model

S = 110.762	R-Sq = 98.12%	R-Sq(adj) = 97.86%
PRESS = 1143944	R-Sq(pred) = 97.50%	

Analysis of Variance

Source	DF	Seq SS	Adj SS	Adj MS	F	P
Regression	10	44904507	44904507	4490451	366.02	0.0000000
F	1	1495426	1495426	1495426	121.89	0.0000000
P	1	2041109	2041109	2041109	166.37	0.0000000
V	1	37456098	37456098	37456098	3053.11	0.0000000
S	1	1276900	1276900	1276900	104.08	0.0000000
FP	1	68168	68168	68168	5.56	0.0212139
FV	1	415707	415707	415707	33.88	0.0000002
FS	1	82530	82530	82530	6.73	0.0115552
PV	1	1188919	1188919	1188919	96.91	0.0000000
VV	1	507438	507438	507438	41.36	0.0000000
VS	1	372213	372213	372213	30.34	0.0000006
Error	70	858773	858773	12268		
Total	80	45763279				

Fits and Diagnostics for Unusual Observations

Obs	w avg	Fit	SE Fit	Residual	St Resid
4	1733.20	1436.04	43.9443	297.161	2.92276R
27	2017.67	1796.79	39.8788	220.873	2.13747R
35	2275.75	2494.69	43.9443	-218.942	-2.15343R
37	1685.41	1418.95	26.1068	266.452	2.47537R
44	1637.25	1917.49	21.3161	-280.235	-2.57827R
53	1250.55	1455.23	42.6322	-204.681	-2.00219R
58	2428.57	2172.94	31.9742	255.630	2.41055R
67	1439.00	1662.03	31.9742	-223.030	-2.10313R
74	1966.40	2183.82	53.2903	-217.422	-2.23917R

R denotes an observation with a large standardized residual.

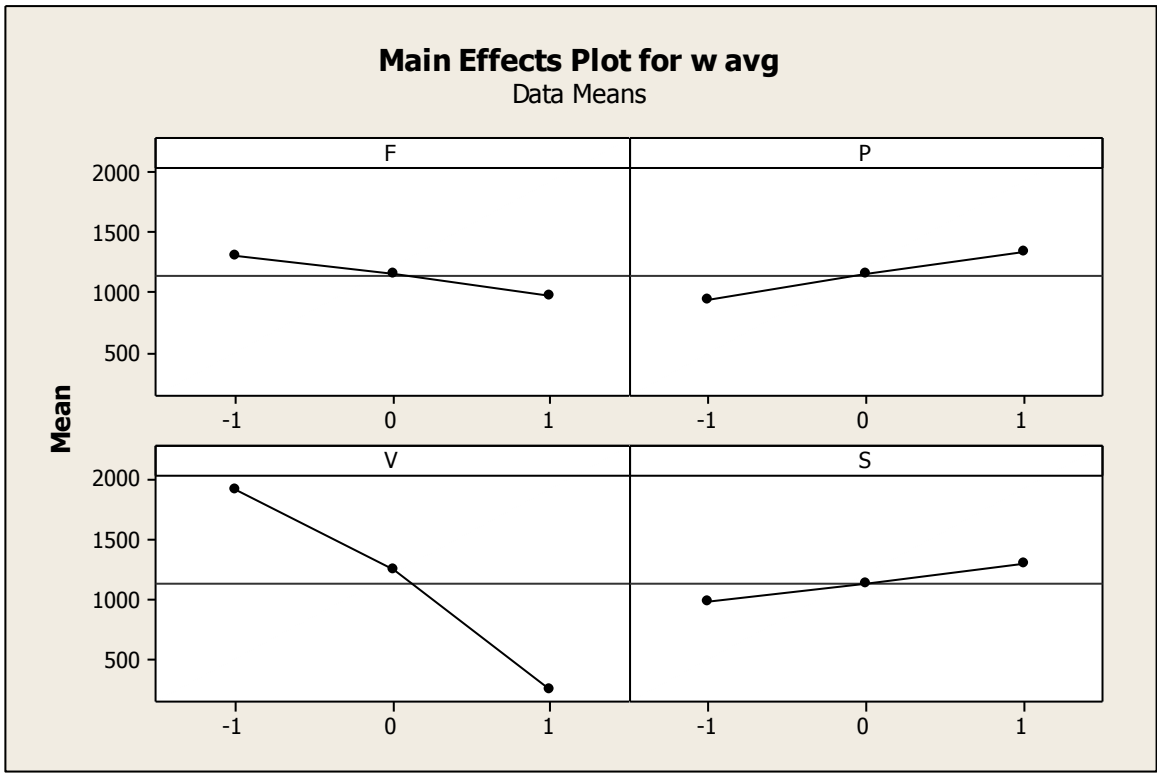

Figure 24: Main effects plots for higher order experiment

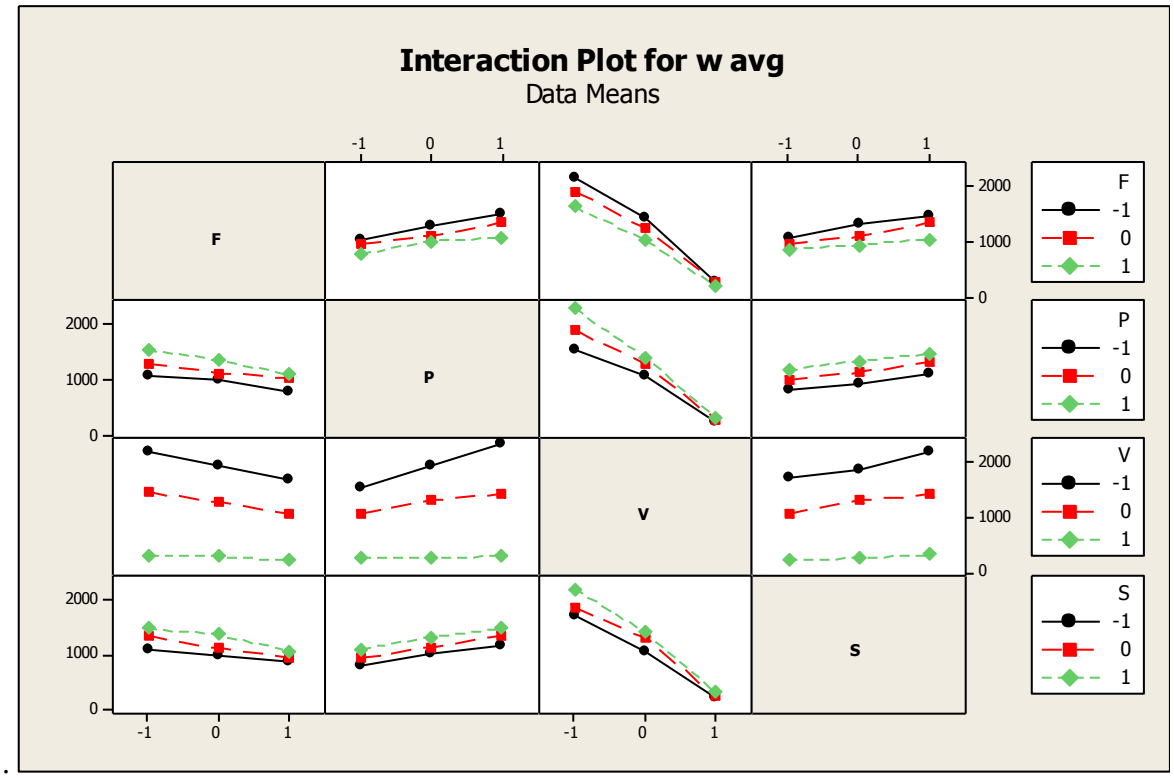

Figure 25: Interaction plots for higher order experiment